

Discrete dislocation plasticity: a simple planar model

This content has been downloaded from IOPscience. Please scroll down to see the full text.

1995 Modelling Simul. Mater. Sci. Eng. 3 689

(<http://iopscience.iop.org/0965-0393/3/5/008>)

View [the table of contents for this issue](#), or go to the [journal homepage](#) for more

Download details:

IP Address: 128.178.146.220

This content was downloaded on 16/06/2014 at 12:33

Please note that [terms and conditions apply](#).

Discrete dislocation plasticity: a simple planar model

Erik van der Giessen[†] and Alan Needleman[‡]

[†] Laboratory for Engineering Mechanics, Delft University of Technology, Delft, The Netherlands

[‡] Division of Engineering, Brown University, Providence, RI 02912, USA

Received 4 January 1995, accepted for publication 27 February 1995

Abstract. A method for solving small-strain plasticity problems with plastic flow represented by the collective motion of a large number of discrete dislocations is presented. The dislocations are modelled as line defects in a linear elastic medium. At each instant, superposition is used to represent the solution in terms of the infinite-medium solution for the discrete dislocations and a complementary solution that enforces the boundary conditions on the finite body. The complementary solution is nonsingular and is obtained from a finite-element solution of a linear elastic boundary value problem. The lattice resistance to dislocation motion, dislocation nucleation and annihilation are incorporated into the formulation through a set of constitutive rules. Obstacles leading to possible dislocation pile-ups are also accounted for. The deformation history is calculated in a linear incremental manner. Plane-strain boundary value problems are solved for a solid having edge dislocations on parallel slip planes. Monophase and composite materials subject to simple shear parallel to the slip plane are analysed. Typically, a peak in the shear stress versus shear strain curve is found, after which the stress falls to a plateau at which the material deforms steadily. The plateau is associated with the localization of dislocation activity on more or less isolated systems. The results for composite materials are compared with solutions for a phenomenological continuum slip characterization of plastic flow.

1. Introduction

Plastic deformation in crystalline metals is a consequence of the motion of large numbers of dislocations, and much is known about dislocation mechanics from both the atomistic and continuum perspectives. However, modeling the behaviour of large numbers of dislocations is a computationally intensive task. Only relatively recently have general analyses of the collective behaviour of discrete dislocations been undertaken. Investigations of dislocation pattern formation and of work-hardening relations in macroscopically homogeneously deformed solids have been carried out where the individual dislocations are described as line singularities in an elastic solid, e.g. by Gulluoglu *et al* [1], Amodeo and Ghoniem [2, 3], Kubin and co-workers [4, 5], Gulluoglu and Hartley [6, 7], Lubarda *et al* [8], Fang and Dahl [9], and Groma and Pawley [10].

On the other hand, conventional phenomenological descriptions of plastic flow are widely used to analyse microscale mechanical processes; examples include deformation and failure in composite materials where the reinforcement dimensions are of the order of micrometres or tens of micrometres, plastic flow near sharp crack tips, micro-indentation, and inhomogeneous grain deformations in polycrystals. Conventional plasticity theories are length-scale independent and are based on the concept of a homogeneously deformed material element. Dislocation based plasticity has a characteristic length, the Burgers vector, and dislocations have a tendency to form highly organized, heterogeneous patterns,

such as cells and walls. Additionally, heterogeneous dislocation arrangements lead to local stress concentrations, e.g., at pile-ups or in dislocation-free regions, that are not modelled by phenomenological characterizations of plastic flow and that can be significant for microscale failure processes. A quantitative characterization of the circumstances under which phenomenological theories of plasticity provide an accurate representation of plastic flow due to dislocation motion remains to be given. This pertains to classical plasticity theories and to theories that incorporate a length scale through the addition of gradient or diffusive terms, e.g. Walgraef and Aifantis [11], Aifantis [12], De Borst [13], Fleck and Hutchinson [14]. What is needed for this characterization, and to provide a method for analysing micro-scale plastic flow processes in circumstances where the discreteness of dislocations plays a dominant role, is a boundary value problem formulation that accounts for discrete dislocation effects.

In this paper, a framework for formulating quasi-static initial/boundary value problems is described where plastic flow arises directly from the collective motion of large numbers of discrete dislocations. Attention is restricted to small strains and the material is characterized in terms of a linear elastic constitutive relation. The dislocations are modelled as line defects in the solid. The solid may consist of more than one phase, as in a composite material, and standard traction and displacement boundary conditions can be enforced to describe the imposed loading. The general formulation applies to three-dimensional solids, but the implementation and examples are for two-dimensional plane strain problems.

The approach that is followed, is based on the formulation of Lubarda *et al* [8], where the stresses and strains are written as superpositions of fields due to the discrete dislocations, which are singular inside the body, and complementary fields that enforce the boundary conditions and any continuity conditions across internal phase boundaries. This leads to a linear elastic boundary value problem for the smooth complementary fields that can be solved by standard numerical techniques such as the finite-element method. Thus, the long-range interactions between dislocations are accounted for through the continuum elasticity fields. Atomistic simulations (Vitek [15], Arias and Joannopoulos [16], Gallego and Ortiz [17]) and experiment (Choi *et al* [18]) show that dislocations are well-represented by the linear elastic fields beyond ten or so atomic distances from the core. In Lubarda *et al* [8], attention was confined to equilibrium dislocation arrangements. Here, drag during dislocation motion, interactions with obstacles and dislocation nucleation and annihilation are accounted for. These involve effects that are not represented by the elasticity description of dislocations and are incorporated into the formulation through a set of constitutive rules.

To demonstrate the potential capabilities of the framework presented here, a number of illustrative boundary value problems are solved for a solid having edge dislocations on a single slip system and being subject to simple shear parallel to the slip direction. Both monophase and composite materials are considered. For the composite material, the same boundary value problem is solved using a phenomenological continuum slip description of plastic flow following the approach of [19]. The phenomenological crystal plasticity and discrete dislocation results for the overall stress-strain response and for the local stress distribution are compared.

The governing equations are formulated using dyadic notation. Vectors and tensors are denoted by bold-face symbols, \cdot denotes the inner product, \otimes the tensor product and $:$ the trace product. For example, with respect to a Cartesian basis e_i and employing the summation convention, $a \cdot b = a_i b_i$, $(a \otimes b)_{ij} = a_i b_j$, $A : B = A_{ij} B_{ji}$ and $(\mathcal{L} : B)_{ij} = \mathcal{L}_{ijkl} B_{lk}$, with summation implied over repeated indices. Latin indices run from 1 to 3, greek indices run from 1 to 2 only. The gradient operator on (tensor) fields

is denoted by ∇ . The second-order unit tensor is I , while \mathcal{I} denotes the fourth-order unit tensor.

2. Discrete dislocation formulation

The problem under consideration is as follows. We consider a linear elastic body of volume V , comprising elastic inclusions with volume V^* , which contains a distribution of dislocations in the matrix material $V^M = V \setminus V^*$ (see figure 1(a)). The elastic properties of the matrix material are governed by the fourth-order tensor \mathcal{L} , while the elastic modulus tensor for the inclusion is denoted by \mathcal{L}^* . The dislocations are regarded as line defects in the elastic continuum (see e.g. [20, 21]). Each dislocation i is characterized by its Burgers vector \mathbf{b}^i and the unit vector \mathbf{n}^i of its slip plane in accordance with the right-hand screw convention for the sense of the dislocation loop, indicated by the unit tangent vector \mathbf{t}^i (see figure 1(b)). This body, with boundary $S = S_u \cup S_f$, is now considered to be subject to time-dependent traction and displacement boundary conditions $\mathbf{T} = \mathbf{T}_0(t)$ on S_f , $\mathbf{u} = \mathbf{u}_0(t)$ on S_u .

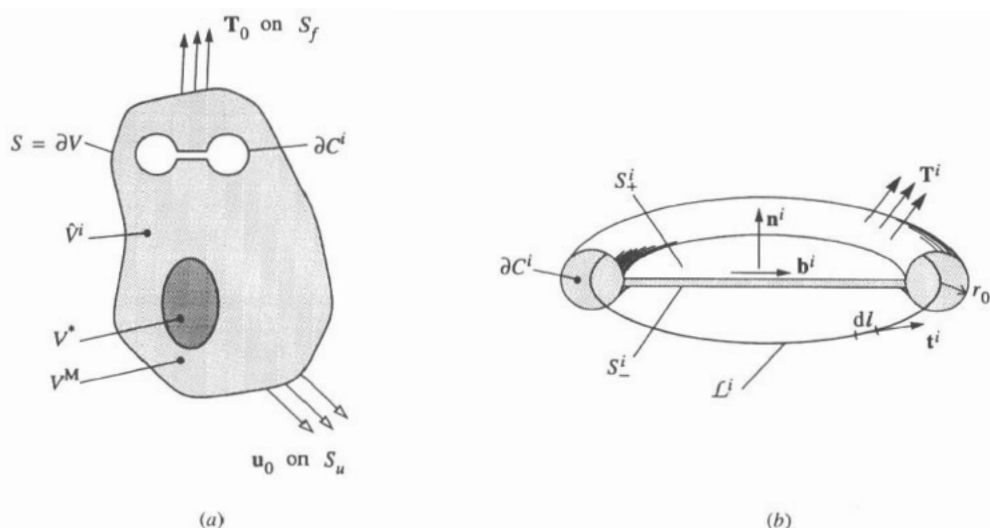


Figure 1. Problem formulation. (a) Body V with inclusions V^* , but with the dislocations removed. (b) Open view of the small core region C^i around dislocation loop i with Burgers vector \mathbf{b}^i . The slip plane normal is \mathbf{n}^i and \mathbf{T} is the surface traction.

We assume the ensuing deformation process to be quasi-static and to involve small strains only. The process will lead to the motion of dislocations, mutual annihilation, the generation of new dislocations and their pinning at point obstacles. The analysis of the deformation process will be performed in an incremental manner in time, where the incremental step at any instant t involves three main computational stages. First, for the current dislocation arrangement, the current stress and strain state of the problem is determined. Secondly, from this state, the so-called Peach–Koehler force, i.e. the driving force for changes in the dislocation structure, is determined. Finally, the instantaneous rate of change of this dislocation structure is computed on the basis of a set of constitutive

equations for the motion, annihilation and generation of dislocations. The first two of these stages will be discussed within a general three-dimensional setting in the next two subsections, and the constitutive equations will be discussed for two-dimensional problems in section 2.3.

2.1. The instantaneous state of the dislocated body

The approach that will be followed to determine the current state of the body with the current instantaneous dislocation distribution is an extension of the formulation of Lubarda *et al* [8] for traction-free solids and that of Blume [22] for general prescribed tractions. Here, we consider mixed traction-displacement boundary conditions, and, more importantly, extend the approach to composite elastic solids.

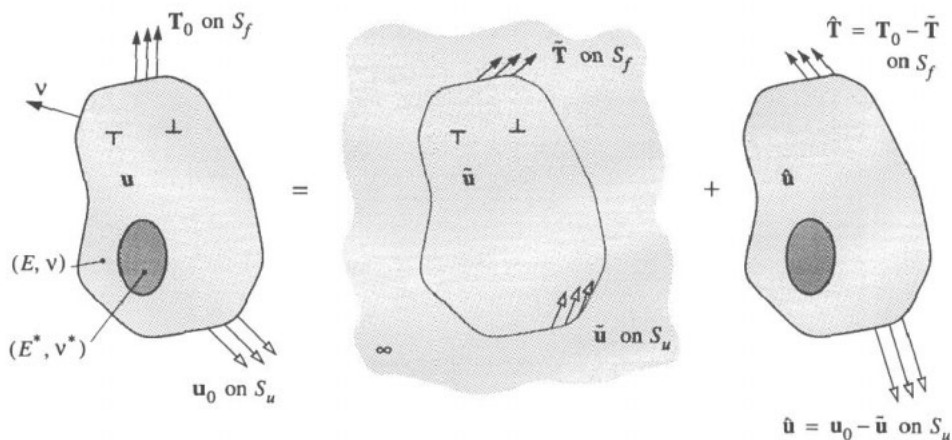


Figure 2. Decomposition of the problem for the dislocated body with inclusions into the problem of interacting dislocations in the homogeneous infinite solid (\sim fields) and the complementary problem for the nonhomogeneous body without dislocations ($\hat{\sim}$ fields).

The current state of the body in terms of the displacement, strain and stress fields is written as the superposition of two fields,

$$u = \tilde{u} + \hat{u} \quad \epsilon = \tilde{\epsilon} + \hat{\epsilon} \quad \sigma = \tilde{\sigma} + \hat{\sigma} \quad \text{in } V \quad (1)$$

respectively, as illustrated in figure 2. The (\sim) fields are the fields associated with the n dislocations in their current configuration but in an infinitely large medium of the homogeneous matrix material (moduli \mathcal{L}). These fields are obtained by superposition of the fields ($u^i, \epsilon^i, \sigma^i$) associated with each individual dislocation,

$$\tilde{u} = \sum u^i \quad \tilde{\epsilon} = \sum \epsilon^i \quad \tilde{\sigma} = \sum \sigma^i \quad (i = 1, \dots, n). \quad (2)$$

Outside a small core region with radius r_0 around each dislocation loop, see figure 1(b), these fields are governed by the standard equations of linear elasticity. The governing equations for the total (\sim) fields can therefore be summarized as

$$\left. \begin{aligned} \nabla \cdot \tilde{\sigma} &= 0 & \tilde{\epsilon} &= \nabla \tilde{u} \\ \tilde{\sigma} &= \mathcal{L} : \tilde{\epsilon} \end{aligned} \right\} \quad \text{in } V = V^M \cup V^* \quad (3)$$

with the following boundary values at the actual boundary S :

$$\begin{aligned} \nu \cdot \tilde{\sigma} &= \tilde{T} & \text{on } S_f \\ u &= \tilde{U} & \text{on } S_u \end{aligned} \quad (4)$$

where ν is the outer unit normal to S . Finding the solution for the (\cdot) fields is facilitated by virtue of the absence of boundaries. In fact, for a number of types of dislocations the infinite-body fields are known analytically and may be found in textbooks (e.g. [20, 21]). However, this is not the case for general curved dislocations and those solutions would have to be obtained.

The (\cdot) fields are the fields to correct for the actual boundary conditions on S as well as for the presence of the inclusions. The governing equations for the corresponding boundary value problem read

$$\left. \begin{aligned} \nabla \cdot \hat{\sigma} &= 0 \\ \hat{\epsilon} &= \nabla \hat{u} \end{aligned} \right\} \quad \text{in } V = V^M \cup V^* \quad (5)$$

$$\begin{aligned} \hat{\sigma} &= \mathcal{L} : \hat{\epsilon} & \text{in } V^M \\ \hat{\sigma} &= \mathcal{L}^* : \hat{\epsilon} + (\mathcal{L}^* - \mathcal{L}) : \tilde{\epsilon} & \text{in } V^* \end{aligned} \quad (6)$$

$$\begin{aligned} \nu \cdot \hat{\sigma} &= \hat{T} = T_0 - \tilde{T} & \text{on } S_f \\ u &= \hat{U} = u_0 - \tilde{U} & \text{on } S_u. \end{aligned} \quad (7)$$

Notice the contribution of the so-called polarization stress

$$\hat{p} = (\mathcal{L}^* - \mathcal{L}) : \tilde{\epsilon} = (\mathcal{L}^* : \mathcal{L}^{-1} - \mathcal{I}) : \tilde{\sigma} \quad (8)$$

to the $\hat{\sigma}$ field in the inclusions (cf. [23]), which is caused by the dislocation strain field and the different elastic properties. With μ and B denoting the shear modulus and bulk modulus of the matrix material, and with μ^* and B^* denoting the corresponding inclusion values, the components of the polarization stress for an isotropic elastic solid are obtained as

$$\hat{p}_{ij} = \left(\frac{\mu^*}{\mu} - 1 \right) \tilde{\sigma}_{ij} + \frac{1}{3} \left(\frac{B\mu^* - \mu B^*}{B\mu} \right) \delta_{ij} \tilde{\sigma}_{kk}$$

in terms of the infinite-body dislocation stresses.

Provided that the dislocation displacement fields remain continuous on S_u and along the interface between the matrix and the inclusion, the (\cdot) fields are smooth. Hence, the equations (5) to (7) constitute a well-posed linear elastic boundary value problem which can be conveniently solved by finite element techniques as in [8].

2.2. The Peach–Koehler force

In an arbitrary state of deformation satisfying the equations (1) to (7), the dislocated body as a whole will not be in thermodynamic equilibrium for any given dislocation structure, due to the strong interaction between dislocations and with the boundary of the body. Non-equilibrium will tend to let the dislocations re-distribute by their motion along the slip systems. The thermodynamic force conjugate to the motion of dislocations is determined by the variation of the potential energy Π of the body, associated with infinitesimal variations of the position δs^i of dislocation i . Writing the potential energy variation in the form

$$\delta \Pi = - \sum_i \int_{\mathcal{L}^i} \mathbf{f}^i \cdot \delta \mathbf{s}^i \, dl \quad (9)$$

\mathbf{f}^i is the so-called Peach–Koehler force.

Many standard references (e.g. [20, 21]) provide elementary treatments of the relationship between the Peach–Koehler force and the local state of a stress in the continuum, including effects of image dislocations to account for boundary conditions, etc. However, the method of solution presented above treats boundary conditions and inclusions in a different manner. Therefore, we consider it appropriate to carefully reconsider here the link with the Peach–Koehler force.

In order to write the potential energy for the dislocated body we follow a dislocation exclusion procedure like that used by Lubarda *et al* [8] and Blume [22]. First we introduce a small core region C^i around each dislocation loop i , which is formed by a torus of radius r_0 along the dislocation line, cut open internally by the slip plane and bounded by two surfaces S_+^i and S_-^i (see figure 1). The total surface of the core region, including S_+^i and S_-^i , is denoted by ∂C^i . Then, the volume of the body excluding the core region C^i is $\hat{V}^i = V \setminus C^i$. The body volume excluding all core regions $\hat{C} = \cup^i C^i$ is $\hat{V} = V \setminus \hat{C}$. The potential energy Π for the dislocated body is then found as the potential energy of the volume \hat{V} excluding all core volumes, while the core energies are accounted for through the work of tractions on the interfaces ∂C^i of \hat{V} . It is shown in appendix A that the superposition of (') and (") fields according to (1) along with (2), gives

$$\begin{aligned} \Pi = & \frac{1}{2} \int_V \hat{\sigma} : \hat{\epsilon} \, dV + \frac{1}{2} \int_V (\hat{\sigma} : \tilde{\epsilon} + \tilde{\sigma} : \hat{\epsilon}) \, dV + \frac{1}{2} \sum_{j \neq k} \sum \int_V \sigma^j : \epsilon^k \, dV \\ & + \sum_i \left[\frac{1}{2} \int_{\hat{V}^i} \sigma^i : \epsilon^i \, dV + \frac{1}{2} \int_{\partial C^i} \mathbf{T}^i \cdot \mathbf{u}^i \, dV \right] - \int_{S_f} \mathbf{T}_0 \cdot (\hat{\mathbf{u}} + \tilde{\mathbf{u}}) \, dS. \quad (10) \end{aligned}$$

Here, \mathbf{T}^i and \mathbf{u}^i are the traction and displacement on ∂C^i due to the corresponding dislocation. The integrals involved in the double summation in (10) represent the interaction energy of the infinite-medium dislocation fields within the finite volume V , while the terms in square brackets represent the self-energy of all dislocations. The interaction energy of the dislocations with the inclusion is incorporated implicitly in the first two volume integrals.

Now, we consider variations of the potential energy in (10) due to variations δs^i of the positions of the dislocations. Such variations lead to variations in the infinite medium displacement fields, $\delta \mathbf{u}^i$, associated with each dislocation and variations in the $\hat{\mathbf{u}}$ displacements, and hence involve strain field variations $\delta \tilde{\epsilon}$ and $\delta \hat{\epsilon}$. A careful analysis of the resulting variations in the potential energy expression, with due consideration of the

singularities at dislocations and the different moduli in matrix and inclusions, is outlined in appendix B. The result is that

$$\delta \Pi = - \sum_i \int_{L^i} [t^i \times (\hat{\sigma} \cdot b^i)] \cdot \delta s^i \, dl - \sum_{j \neq k} \int_{L^k} [t^k \times (\sigma^j \cdot b^k)] \cdot \delta s^k \, dl \quad (11)$$

so that the Peach–Koehler force f^i acting on the i th dislocation is found from (9) as

$$f^i = t^i \times \left[\left(\hat{\sigma} + \sum_{j \neq i} \sigma^j \right) \cdot b^i \right].$$

The component f^i of the Peach–Koehler force in the direction $t^i \times n^i$ in the slip plane and normal to the dislocation is found as

$$f^i = n^i \cdot \left(\hat{\sigma} + \sum_{j \neq i} \sigma^j \right) \cdot b^i. \quad (12)$$

It is this component of the Peach–Koehler force that will determine the motion of the dislocation in its slip plane, as will be discussed in the next section. In [8] this force, or in fact the total resultant force and associated moment on a dislocation line, was used to determine equilibrium configurations of a given set of dislocations. The analysis here confirms the validity of the expression (12), even for boundary value problems with mixed traction–displacement boundary conditions and in the presence of inclusions.

2.3. Constitutive equations for motion, creation and annihilation

In what follows, we confine attention to plane-strain problems involving edge dislocations, viewed in a direction perpendicular to the dislocation lines. In fact, we consider pairs of edge dislocations, each pair in a limiting sense representing a cross-section of a dislocation loop. The dislocations in such a dipole have opposite signs, and this is commonly incorporated through the use of the signed length of the Burgers vector $b^i = (b^i \times t^i) \cdot n^i$ ($i = 1, \dots, n$). The plane of deformation is the x_1 – x_2 plane, and in this paper all slip planes are taken to be parallel to the x_1 axis. If the material is elastically isotropic with shear modulus μ and Poisson's ratio ν , the components u_α^i ($\alpha = 1, 2$) of the infinite-body displacement field $u^i(x_\alpha)$ due to dislocation i positioned at (X_1^i, X_2^i) are given by (e.g. [20, 21])

$$u_1^i(x_\alpha) = \frac{b^i}{2\pi(1-\nu)} \left\{ \frac{1}{2} \frac{\Delta x_1 \Delta x_2}{(\Delta x_1)^2 + (\Delta x_2)^2} - (1-\nu) \tan^{-1} \left(\frac{\Delta x_1}{\Delta x_2} \right) \right\} \quad (13)$$

$$u_2^i(x_\alpha) = \frac{b^i}{2\pi(1-\nu)} \left\{ \frac{1}{2} \frac{(\Delta x_2)^2}{(\Delta x_1)^2 + (\Delta x_2)^2} - \frac{1}{4} (1-2\nu) \ln \frac{(\Delta x_1)^2 + (\Delta x_2)^2}{(b^i)^2} \right\} \quad (14)$$

where

$$\Delta x_\alpha = x_\alpha - X_\alpha^i \quad (\alpha = 1, 2).$$

The corresponding in-plane stress field components $\sigma_{\alpha\beta}^i$ read [20, 21]

$$\sigma_{11}^i(x_\alpha) = - \frac{\mu b^i}{2\pi(1-\nu)} \frac{\Delta x_2 [3(\Delta x_1)^2 + (\Delta x_2)^2]}{[(\Delta x_1)^2 + (\Delta x_2)^2]^2} \quad (15)$$

$$\sigma_{22}^i(x_\alpha) = \frac{\mu b^i}{2\pi(1-\nu)} \frac{\Delta x_2[(\Delta x_1)^2 - (\Delta x_2)^2]}{[(\Delta x_1)^2 + (\Delta x_2)^2]^2} \quad (16)$$

$$\sigma_{12}^i(x_\alpha) = \frac{\mu b^i}{2\pi(1-\nu)} \frac{\Delta x_1[(\Delta x_1)^2 - (\Delta x_2)^2]}{[(\Delta x_1)^2 + (\Delta x_2)^2]^2}. \quad (17)$$

For such two-dimensional problems, we consider the following ingredients to the evolution of the dislocation structure during the deformation process: the motion of dislocations along their slip plane, pinning of dislocations at obstacles, annihilation of opposite dislocations, and generation of new dislocation pairs from discrete sources. Similar mechanisms have been considered in previous two-dimensional studies (e.g. [1, 2, 3, 6, 7]), as well as in the three-dimensional simulations of Kubin *et al* [5], although the specific constitutive rules that have been implemented differ.

The motion of the i th dislocation is controlled by the in-plane component f^i of the Peach-Koehler force according to (12). For edge dislocations this component reduces to

$$f^i = \tau^i b^i$$

where τ^i is the resolved shear stress acting in the slip plane at the dislocation line, defined by

$$\tau^i = n^i \cdot \left(\hat{\sigma} + \sum_{j \neq i} \sigma^j \right) \cdot m^i$$

with m^i denoting the unit vector along the slip plane of dislocation i . Here, the velocity v^i of a dislocation in the direction of m^i is taken to be related linearly to the resolved shear stress through the linear drag relation

$$\tau^i b^i = B v^i \quad (18)$$

where B is the drag coefficient. For metals, the major contribution stems from phonon drag, while for nonmetallics, there may be an increasing contribution to B from the Peierls barrier (see e.g. [21]). A similar relationship has been adopted in other quasi-static analyses [1-3, 9, 10], while in the truly dynamic analyses in [6, 7] a corresponding damping force has been taken into account.

The motion of dislocations along a slip plane can be hindered in real crystals by several types of obstacles, such as dislocations on intersecting slip planes, small precipitates, etc. In two dimensions, we model this by means of point obstacles at which moving dislocations get pinned. Such pinned dislocations are usually the origin of dislocation pile-ups. As the number of dislocations in a pile-up increases, the shear stress acting on the leading dislocation increases substantially, so that it will eventually bypass the obstacle through a thermally activated process. We model this by releasing the pinned dislocation once its resolved shear stress exceeds (in absolute value) the obstacle's strength τ_{obs} .

Two edge dislocations with opposite Burgers vector (dipoles) will annihilate each other when they are brought closer and closer together. Presumably the destruction of dipoles is due to the effect of their self-stresses. It is modelled here very simply in the way

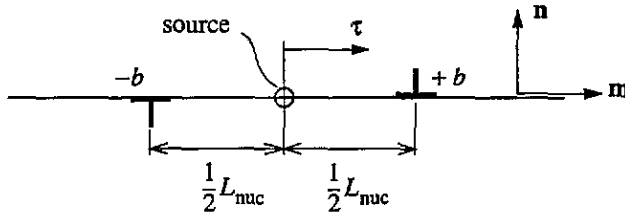


Figure 3. The two-dimensional dislocation source with Burgers vector b on slip plane with normal n and slip direction m generates a dislocation dipole at mutual distance of L_{nuc} . If the resolved shear stress $\tau > 0$, a positive dislocation ($b > 0$) is generated in the direction of m ; the dislocation signs change when $\tau < 0$.

that annihilation is taken to occur when opposite dislocations have approached within a material-dependent, critical annihilation distance L_e .

New dislocation are being generated through the operation of Frank–Read sources. The initial dislocation segment of a Frank–Read source bows out until a critical Frank–Read configuration is formed and leaves behind a replica of itself. Thus, a source is characterized by the critical stress for activation of the Frank–Read process, the time to form a critical configuration and the diameter of the generated dislocation loop. The values of these three variables depend on the length of the initial Frank–Read segment, the elastic properties and the drag coefficient. Implementing this process in two dimensions clearly involves idealizations and approximations. The way we treat dislocation nucleation is to assume that sources are point sources on the slip plane, which generate a dislocation dipole when the magnitude of the shear stress at the source, $|\tau|$, has exceeded the critical stress τ_{nuc} during a period of time t_{nuc} . The dipole comprises two opposite dislocation with Burgers vector $\pm b$, with the polarity being determined by the sign of τ (see figure 3). The distance L_{nuc} between the two dislocations is taken to be determined by the critical stress according to

$$L_{\text{nuc}} = \frac{\mu}{2\pi(1-\nu)} \frac{b}{\tau_{\text{nuc}}}.$$

This ensures that, when the new dipole is generated, the total resolved shear stress τ_{nuc} balances the attractive shear stress that the two dislocations exert on one another (see (17) for $\Delta x_1 = L_{\text{nuc}}$, $\Delta x_2 = 0$).

3. Formulation of two-dimensional unit cell analyses

We demonstrate the approach outlined in the previous sections by considering the boundary value problem illustrated in figure 4. The material is assumed to be built up of a doubly periodic array of unit cells of width $2w$ and height $2h$. In some computations, the unit cell will be assumed to contain a central (dislocation-free) inclusion of size $2w_f$ by $2h_f$. The cell is subjected to simple shear deformations, prescribed through the kinematic boundary conditions

$$\left. \begin{aligned} u_{0,1}(t) &= \pm h \dot{\Gamma} t \\ u_{0,2}(t) &= 0 \end{aligned} \right\} \quad \text{along } x_2 = \pm h$$

where $\dot{\Gamma}$ is the applied shear rate. Periodic boundary conditions are imposed along the lateral sides $x_1 = \pm w$. The average shear stress $\bar{\tau}$ needed to sustain the deformation is

computed from the shear component σ_{12} of the total stress σ according to (1), either along the top or the bottom face of the region:

$$\bar{\tau} = \frac{1}{2w} \int_{-w}^w \sigma_{12}(x_1, \pm h) dx_1.$$

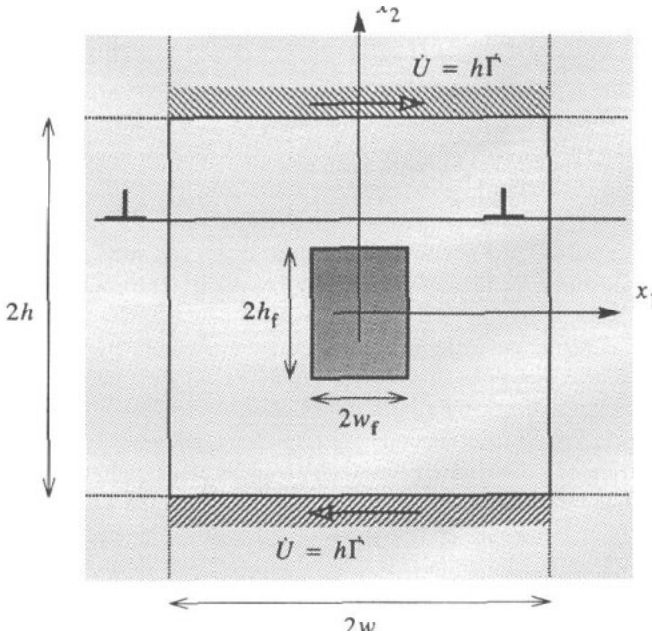


Figure 4. Unit cell in a doubly periodic array, subjected to simple shear. All slip planes are taken to be parallel to the shear direction (x_1).

As mentioned before, dislocation motion on a number of slip planes will be considered that are parallel to the x_1 axis. All dislocations come in pairs, or dipoles, with opposite signs of their Burgers vectors, so that the net Burgers vector is zero. For simplicity all dislocations are taken to have the same magnitude b of the Burgers vector. The determination of the (σ) fields is somewhat involved for such periodic cell problems. For each dislocation in the unit cell, one must also account for the fields due to its replicas in all other cells in the array. Even though the self-stress fields rapidly decay with the distance from the dislocation, arrays of dislocations have been observed to give rise to very long-range effects (e.g., [1] and [8]). Moreover, Gulluoglu *et al* [1] noted that the truncation of the number of adjacent replicas may give rise to artificial dislocation wall formation. In order to resolve this problem, it was suggested in [1] to first perform the summation over the infinitely long column of dislocations, obtained by collecting all replicas of the dislocation along the x_2 direction, followed by the summation of the results for such columns along the x_1 direction. For such a column of dislocations, or dislocation wall, analytical solutions are available in the literature for the infinite-medium fields (see e.g. also [20]). The summation of these dislocation wall fields for a number of replicas left and right of the cell converges rapidly [1]. However, this approach has proved to be not particularly suited to the present boundary

value problem, since that summation for any finite number of replicas gives different stress and displacement fields along the left ($x_1 = -w$) and right ($x_1 = w$) cell boundaries so that exact periodicity is difficult to realize.

In this work we have therefore chosen a different approach in which the summation is first carried out over replicas of each dislocation on the same slip plane. Then, the fields due to such infinitely long strings of dislocations are summed over replicas of the slip plane above and below the cell. It is shown in some detail in appendix C that the stress field of string i , i.e. dislocation i inside the cell and its replicas at mutual distance $2w$ on the same slip plane, can be determined analytically, yielding:

$$\sigma_{11}^i(x_\alpha) = -\frac{\mu}{2\pi(1-\nu)} \frac{\pi b^i}{2w} \frac{1}{\cosh \pi \Delta \xi_2 - \cos \pi \Delta \xi_1} \times \left\{ 2 \sinh \pi \Delta \xi_2 + \pi \Delta \xi_2 \frac{1 - \cos \pi \Delta \xi_1 \cosh \pi \Delta \xi_2}{\cosh \pi \Delta \xi_2 - \cos \pi \Delta \xi_1} \right\} \quad (19)$$

$$\sigma_{22}^i(x_\alpha) = \frac{\mu}{2\pi(1-\nu)} \frac{\pi b^i}{2w} \left\{ \pi \Delta \xi_2 \frac{1 - \cos \pi \Delta \xi_1 \cosh \pi \Delta \xi_2}{(\cosh \pi \Delta \xi_2 - \cos \pi \Delta \xi_1)^2} \right\} \quad (20)$$

$$\sigma_{12}^i(x_\alpha) = \frac{\mu}{2\pi(1-\nu)} \frac{\pi b^i}{2w} \frac{\sin \pi \Delta \xi_1}{\cosh \pi \Delta \xi_2 - \cos \pi \Delta \xi_1} \times \left\{ 1 - \pi \Delta \xi_2 \frac{\sinh \pi \Delta \xi_2}{\cosh \pi \Delta \xi_2 - \cos \pi \Delta \xi_1} \right\} \quad (21)$$

where

$$\Delta \xi_\alpha = (x_\alpha - X_\alpha^i)/w \quad (\alpha = 1, 2). \quad (22)$$

The summation of the displacement field of dislocation string i needs special consideration in view of the discontinuities in u_1 (see (13)) and the fact that u_2 is unbounded for $(\Delta x_1)^2 + (\Delta x_2)^2 \rightarrow \infty$ (see (14)). The mathematical difficulties associated with this are eliminated by not considering individual dislocations, but dipoles. After having performed the summation over a string of such dipoles, the individual fields can be recovered and written in the following form (see appendix C):

$$u_1^i(x_\alpha) = \frac{b^i}{2\pi(1-\nu)} \left\{ \frac{1}{4} \frac{\pi \Delta \xi_2 \sin \pi \Delta \xi_1}{\cosh \pi \Delta \xi_2 - \cos \pi \Delta \xi_1} - (1-\nu) \tan^{-1} \left(\frac{\tan \pi \Delta \xi_1/2}{\tanh \pi \Delta \xi_2/2} \right) \right\} - \frac{b^i}{2} \delta^i \operatorname{sgn}(\Delta \xi_2) \quad (23)$$

$$u_2^i(x_\alpha) = \frac{b^i}{2\pi(1-\nu)} \left\{ \frac{1}{4} \frac{\pi \Delta \xi_2 \sinh \pi \Delta \xi_2}{\cosh \pi \Delta \xi_2 - \cos \pi \Delta \xi_1} - \frac{1}{4} (1-2\nu) \ln(\cosh \pi \Delta \xi_2 - \cos \pi \Delta \xi_1) \right\}. \quad (24)$$

The term with δ^i in (23) ensures that the solution is valid for all $\Delta \xi_1 \in (-1, 1)$, i.e. for all $x_1 - X_1^i \in (-w, w)$, by letting

$$\delta^i = \begin{cases} -1 & \text{if } \Delta \xi_1 \in (-3/2, -1/2) \\ +1 & \text{if } \Delta \xi_1 \in (1/2, 3/2). \end{cases}$$

The stress and displacement fields due to all replicas of dislocation i are to be determined by summation of these fields for infinite strings of dislocations, equations (19)–(21) and (23)–(24), in the x_2 direction. Fortunately, these infinite string fields decay nearly exponentially with $\Delta\xi_2$. It has been found that only three strings on either side of the central string need to be considered for excellent convergence.

Finally, because of periodicity, dislocations leaving the cell at $x_1 = \pm w$ re-enter at the opposite side $x_1 = \mp w$. Only the displacement fields of the dislocation need to be corrected for that by adding the contribution

$$\begin{aligned} u_1^i(x_\alpha) &= \frac{b^i}{2} \delta^i \operatorname{sgn}(\Delta x_2) \\ u_2^i(x_\alpha) &= 0. \end{aligned} \quad (25)$$

The step in the displacements in (25) is retained at all times even after dislocation i has annihilated with another dislocation.

It is noted that in [24] we have presented a few results for a different problem, where the sides $x_1 = \pm w$ are traction-free, as a further illustration of the solution procedure for boundary value problems outlined in section 2. In those analyses, attention was confined to monophase materials, but that is not a necessary restriction.

A standard finite-element technique is used to solve the elastic boundary value problem (5)–(7). Here, four-noded quadrilateral elements with four Gauss integration points are used. The polarization stress \hat{p} according to (8) is accounted for as a body force to be evaluated at each integration point. The infinite-medium tractions \tilde{T} on S_f are computed in separate Gaussian integration points along element edges at S_f , while the corresponding displacements \tilde{U} are evaluated at the nodal points on S_u .

The deformation process is solved in a linear incremental manner, using an Euler forward time-integration scheme of the equations of motion (18). The algorithm is similar in spirit to the dislocation dynamics procedure proposed by Amodeo and Ghoniem [2, 3], but the details are somewhat different. An adaptive time-stepping algorithm is used that ensures that the flight distance of any dislocation during a time step Δt remains smaller than a user-defined maximum distance Δs_{\max} . In the computations to be presented here, we have used values of Δs_{\max} ranging from $0.16d$ to $0.3d$, where d is the spacing between slip planes. The time step is also adapted to the time scale of nucleation events, determined by time laps t_{nuc} . For each slip plane, within each time increment, a subincremental technique is used to update all dislocation positions, giving due attention to possible annihilation or pinning. In order to avoid numerical instabilities, a suitable amount of underrelaxation is used for dislocation pile-ups.

4. Continuum formulation

For comparison purposes, calculations are carried out for the plane strain unit cell in figure 4 using continuum slip plasticity to describe the material response. Overviews of the continuum slip formulation and its physical background are given in Asaro [25], Bassani [26] and Cuitiño and Ortiz [27]. As in Peirce *et al* [19], the numerical analyses are based on a finite-strain Lagrangian convected coordinate formulation of the field equations. However, attention here is confined to small strains and finite strain effects are negligible. For simplicity, only the small displacement gradient form of the governing equations is presented.

The discretization is based on the rate principle of virtual work

$$\int_V \dot{\sigma} : \delta \dot{\epsilon} dV = \int_{S_f} \dot{T}_0 \cdot \delta u dS \quad (26)$$

where $(\dot{})$ denotes $\partial()/\partial t$.

The crystal is taken to have one slip system, with the slip plane normal parallel to the x_2 axis and with the slip direction parallel to the x_1 axis. The plastic strain rate, $\dot{\epsilon}^p$, is then written as

$$\dot{\epsilon}^p = \frac{\dot{\gamma}}{2} (m \otimes n + n \otimes m) \quad (27)$$

where m is the slip direction and n is the slip plane normal. The total strain rate, $\dot{\epsilon}$, is

$$\dot{\epsilon} = \dot{\epsilon}^e + \dot{\epsilon}^p \quad (28)$$

where the elastic strain rate, $\dot{\epsilon}^e$, is given in terms of the stress rate, $\dot{\sigma}$, by Hooke's law

$$\dot{\epsilon}^e = \mathcal{L}^{-1} : \dot{\sigma}. \quad (29)$$

Combining (27), (28) and (29), and inverting to obtain the stress rate-strain rate relation gives

$$\dot{\sigma} = \mathcal{L} : \left[\dot{\epsilon} - \frac{\dot{\gamma}}{2} (m \otimes n + n \otimes m) \right]. \quad (29)$$

The material is taken to be viscoplastic, with the strain rate given by the power-law relation

$$\dot{\gamma} = \dot{a} \left(\frac{\tau}{g} \right) \left(\left| \frac{\tau}{g} \right| \right)^{(1/m)-1}. \quad (31)$$

g is the slip system hardness, and the slip system resolved shear stress, τ , is simply σ_{12} . The slip system strain hardening is described by

$$\tau(\gamma) = \tau_0 (\gamma/\gamma_0 + 1)^N \quad (32)$$

where τ_0 is the slip system strength, γ_0 is a reference strain and N is the strain hardening exponent.

The unit cell is subject to prescribed displacement rates

$$\left. \begin{aligned} \dot{u}_{0,1} &= \pm h \dot{\Gamma} \\ \dot{u}_{0,2} &= 0 \end{aligned} \right\} \quad \text{along } x_2 = \pm h \quad (33)$$

corresponding to a shear rate $\dot{\Gamma}$, with the height of the cell, $2h$, fixed. Periodic boundary conditions are imposed along the lateral sides $x_1 = \pm w$ by taking $\dot{u}_i(x_2, w) = \dot{u}_i(x_2, -w)$ for $i = 1, 2$.

The deformation history is calculated in a linear incremental manner. In order to increase the stable time step, a rate tangent modulus method, as described in Peirce *et al* [19], is used. The finite-element discretization is based on quadrilateral elements consisting of four 'crossed' linear displacement triangles.

5. Results for monophasic material

In this section we present the results of a number of selected studies carried out by means of the unit cell problem outlined in section 3. All results are for square unit cells, $w = h$ (see figure 4), containing 80 equally spaced slip planes. Poisson's ratio is $\nu = 0.3$. The half-width of the cell relative to the Burgers vector b of the dislocations is given by $w = 4000b$ (with $b = 2.5 \times 10^{-10}$ m, the Burgers vector for copper as a representative parameter value, the cell size is $4 \mu\text{m}^2$). The annihilation distance is taken as $L_e = 6b$. The coefficient B in the drag relationship (18) is specified relative to the applied shear rate $\dot{\Gamma}$ through the dimensionless number $B\dot{\Gamma}/\mu = 0.38 \times 10^{-11}$ (taking $\mu = 0.26 \times 10^5$ MPa and $B = 10^{-4}$ Pa s as representative parameter values for aluminium [5], this corresponds to a shear rate of $\dot{\Gamma} = 10^3 \text{ s}^{-1}$). Unless noted otherwise, all obstacles in these computations are taken to have the same strength $\tau_{\text{obs}} = 5.7 \times 10^{-3} \mu$. The assumed nucleation properties will be discussed shortly.

5.1. Initially dislocation-free material

We start out by briefly considering a material that is initially completely free of dislocations, but that contains a distribution of dislocation sources and obstacles. Upon straining, all sources will start to generate dislocations at the same instant if the sources are assumed to have the same strength, since the stress distribution prior to the moment is completely uniform. Apart from being computationally inconvenient, such a burst of dislocations is not very realistic. Therefore, we select the strength of the sources randomly from a Gaussian strength distribution. All results to be presented in this paper are for a mean strength $\bar{\tau}_{\text{nuc}} = 1.9 \times 10^{-3} \mu$, corresponding to a mean nucleation distance of $L_{\text{nuc}} = 125b$, while the nucleation time is taken as $t_{\text{nuc}} = 2.6 \times 10^6 B/\mu$ (or $t_{\text{nuc}} = 10^{-5}/\dot{\Gamma}$). Unless noted otherwise, the strength distribution is assumed to have a standard deviation of $0.2\bar{\tau}_{\text{nuc}}$.

When the material is deformed in simple shear, the uniform stress $\hat{\sigma}$ increases linearly with Γ , until at some instant the resolved shear stress τ reaches the lowest critical value τ_{nuc} for any of the sources. When, after an elapse of t_{nuc} , the first dipole is actually generated, the total stress field $\hat{\sigma} + \tilde{\sigma}$ in the unit cell ceases to be homogeneous. Upon continued deformation, the dislocations will move along their slip plane, and the total stress field continuously changes until the critical strength is exceeded again for some dislocation source, and so forth. Once the dislocation density attains a certain level, the dislocation stress fields become increasingly important in determining the resolved shear stresses at dislocation sources. This tends to become a self-reinforcing phenomenon that leads to the formation of dislocation pile-ups on specific slip planes, and to localization of the dislocation activity on a few slip planes. An example of this is depicted in figure 5(a), showing two distinct 'bands' in which dislocation motion is responsible entirely for further plastic deformation. The phenomenon may be expected to depend on the standard deviation in the distribution of the strengths of the sources.

As an illustration, figure 5(b) shows the dislocation distribution at the same shear strain when, for the same distribution of sources and obstacles, and for the same average strength, the standard deviation of the strength distribution was taken to be smaller, i.e. $0.1\bar{\tau}_{\text{nuc}}$. With the smaller standard deviation, the distribution of the source strengths is more uniform. Hence, in figure 5(b), when dislocation nucleation begins at one source the stress fields from the nucleated dislocations trigger nucleation at nearby sources and slip activity tends to localize near one slip plane. When the source strength distribution is less uniform, as in figure 5(a), there is a greater likelihood of a weak source away from the initial one being activated before the dislocation stress fields associated with initial source have induced substantial further nucleation.

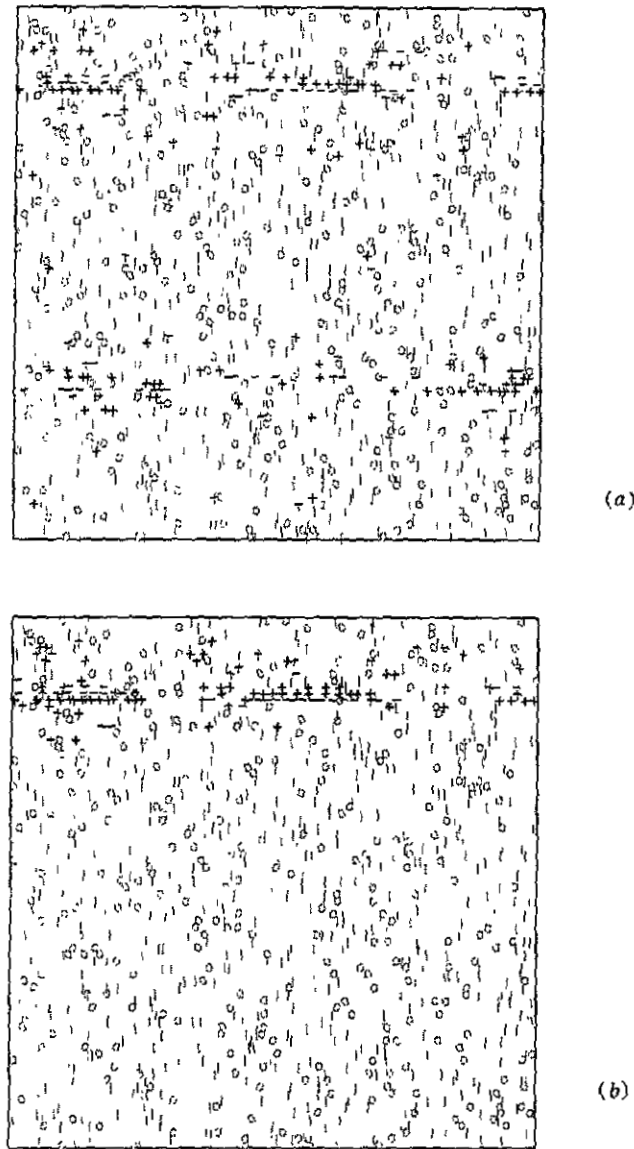


Figure 5. Dislocation distributions in an initially dislocation-free, homogeneous material at $\Gamma = 0.44\%$ for two different standard deviations in the strength distribution of dislocation sources, namely (a) $0.2\epsilon_{nuc}$, (b) $0.1\epsilon_{nuc}$. The + denotes a positive dislocation while the - denotes a negative dislocation. The grey | and \circ denote obstacles and dislocation sources, respectively.

5.2. Material with initial dislocations

As mentioned before, dislocations on a slip system may act as obstacles for the motion of dislocations on other slip systems. This is due to the strong interactions between the two families of dislocations. It has long been known (e.g. [28, 29]) that this is the reason for the high stage-II hardening rate in crystals caused by the possibility of secondary slips. Dislocation motion on the primary slip system is then severely hindered by the presence of

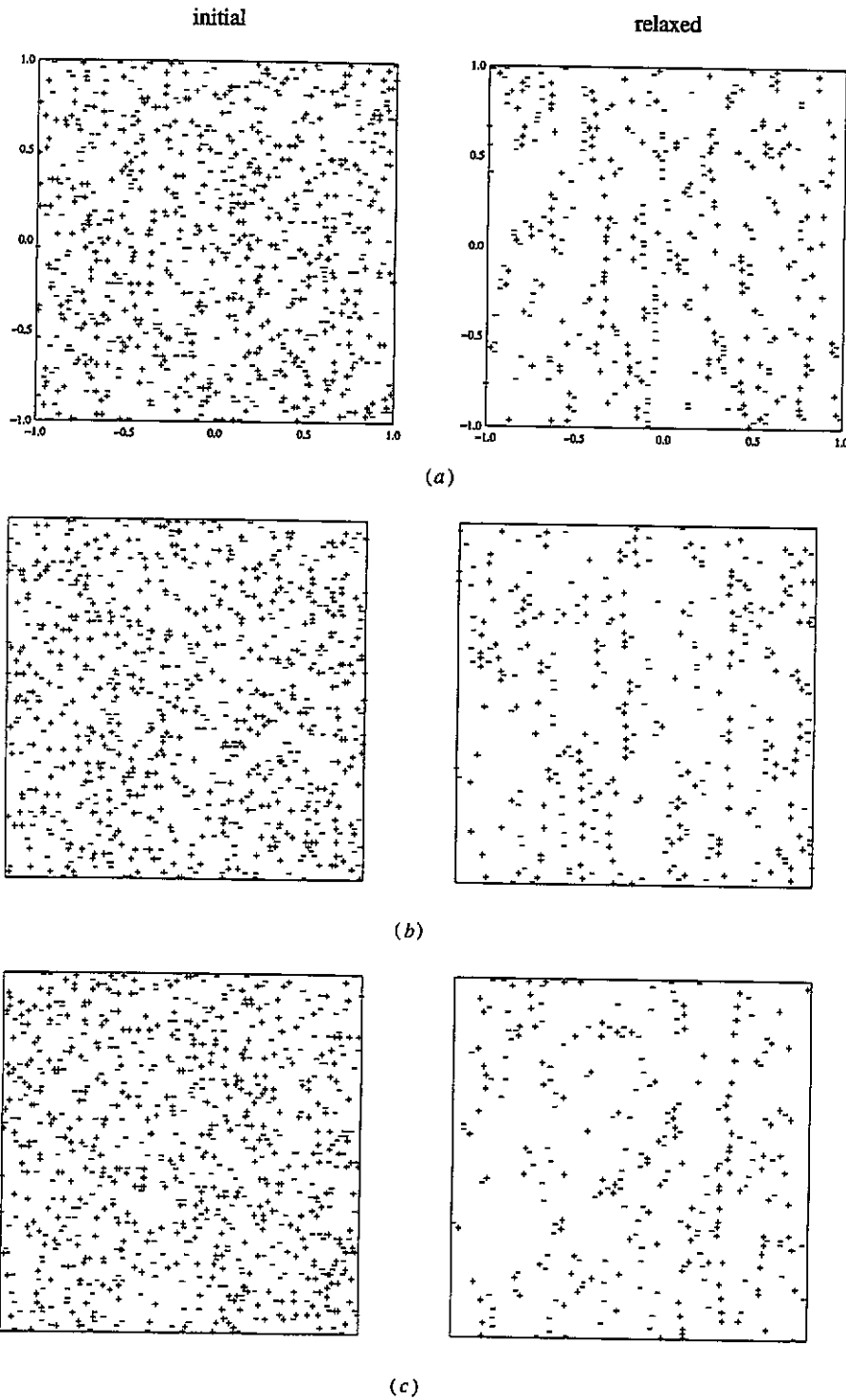


Figure 6. Initially random dislocation distributions and corresponding equilibrium distributions after relaxation, for three different random realizations (a) to (c).

dislocations on the secondary slip systems.

These effects would emerge clearly, for instance, when we imagine a crystal to be deformed first so that one slip system is mainly activated, unload the material and subsequently load the material in a different direction so that slip occurs only on another slip system. In an attempt to mimic this within the current model with just one slip system, we perform the following simulation. First, we randomly introduce dipoles of dislocations, which we then let relax (under fixed displacements, $\Gamma = 0$). Next, we add randomly generated obstacles and sources. This then forms the initial state of the material that is to be subjected to simple shear. As the number of sources and obstacles is kept constant during the simulation, the results to be presented highlight the influence of the strength and density of these entities. On the other hand, for real metals during stage-II hardening, the density of sources and, especially, of obstacles will generally increase with deformation.

Figure 6 shows three random, initial dislocation distributions as well as the corresponding relaxed configuration. For all three cases, the initial dislocation density is $200/hw$ (with $h = w = 1 \mu\text{m}$ this corresponds to a dislocation density of $2 \times 10^{10} \text{ cm}^{-2}$); the densities of the relaxed configurations are: (a) $93/hw$, (b) $85/hw$ and (c) $68/hw$.

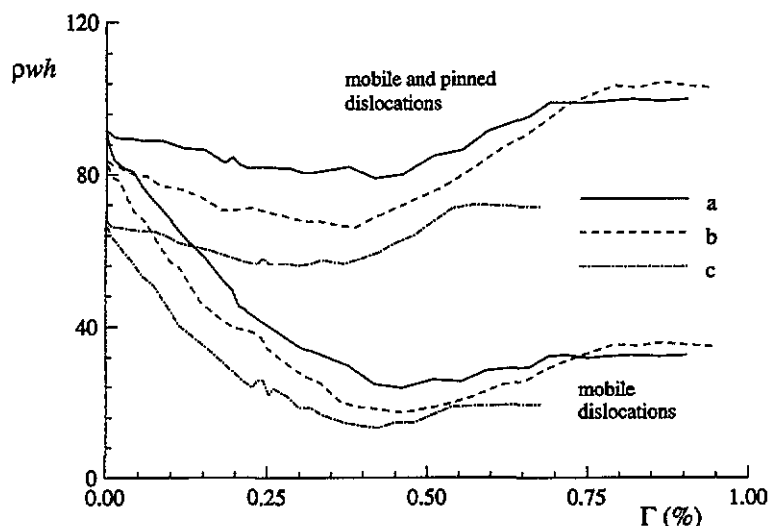


Figure 7. Evolution of total and mobile dislocations during simple shear simulations starting from each of the three relaxed configurations shown in figure 6(a) to (c).

In each of these three relaxed configurations, dislocation sources and obstacles are then generated randomly. The density of sources in all three cases is taken as $\rho_{\text{nuc}} = 80/hw$ (i.e. of the same order of magnitude as the relaxed dislocation density), while an obstacle density of $\rho_{\text{obs}} = 160/hw$ is assumed. Now, on shearing the material, the relaxed dislocation structures gradually evolve when the dislocations start to move and annihilate with each other or with freshly generated dislocations. The evolution of the dislocation densities for each of the simulations starting from the three relaxed configurations in figure 6 is shown in figure 7. It is seen that the relaxed dislocation structure is broken down upon shearing, and that in the early stages of the deformation, the total dislocation densities decrease by around 15 %. The density of mobile dislocations falls much more due to the fact that many dislocations get pinned at obstacles. After some deformation, the rate of nucleation of new

dislocations exceeds the rate of annihilation and pinning, so that the dislocation densities (total as well as mobile) start to increase. However, the two rates do not differ much, and especially the mobile dislocation density increases only somewhat with deformation. During these stages of deformation, dislocation pile-ups are formed on specific slip planes, leading to localization of the slip activity on a few slip planes, as noted before in relation to figure 5. Eventually a 'steady state' is reached where the dislocation structures remain essentially the same. These structures, corresponding to the above three relaxed configurations, are shown in figure 8.

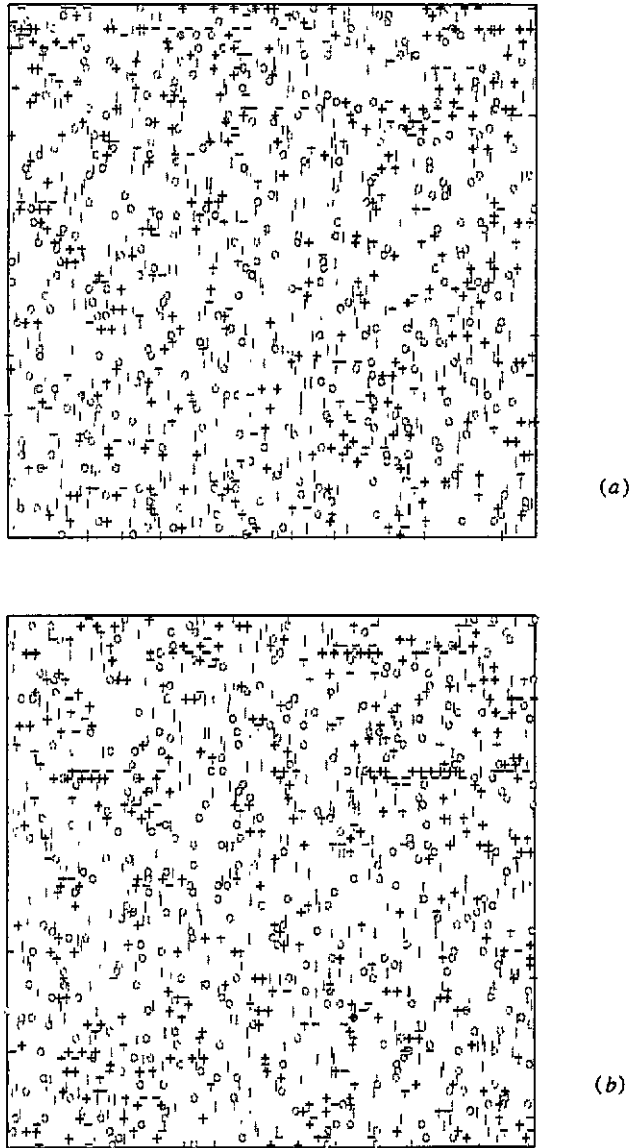


Figure 8. Dislocation distributions for each of three relaxed configurations shown in figure 6(a) to (c), respectively, after shearing to (a) $\Gamma = 0.91\%$, (b) $\Gamma = 0.90\%$, (c) $\Gamma = 0.68\%$.

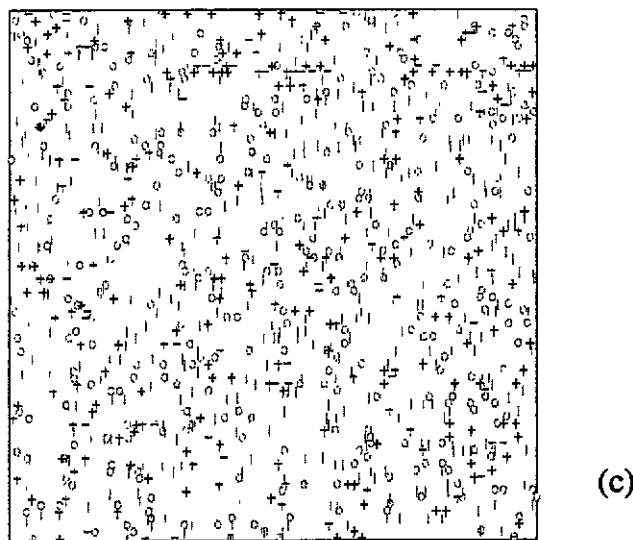


Figure 8. (Continued)

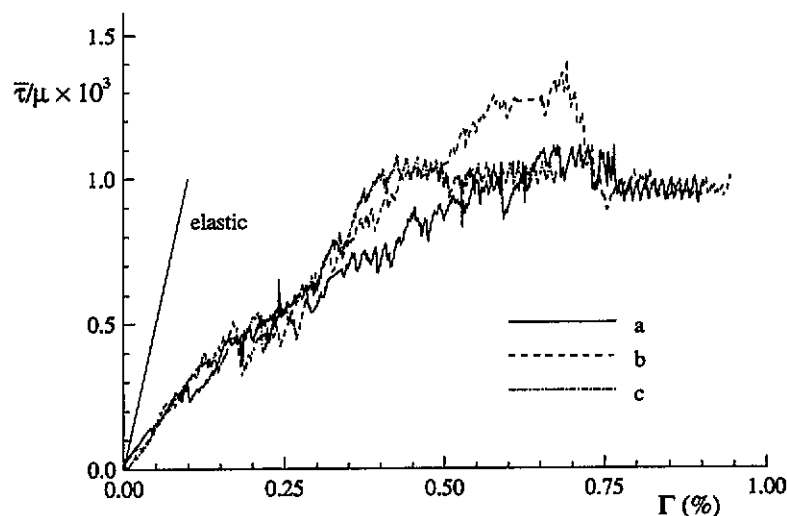


Figure 9. Overall shear stress response to simple shear deformations starting from each of the three relaxed configurations shown in figure 6(a) to (c). The deformed dislocation configurations are shown in figure 8(a) to (c). The grey line would correspond to a purely elastic response.

Figure 9 shows the shear stress responses during simple shearing for each of the three cases. Due to the presence of initial mobile dislocations, the responses do not show an elastic regime. Up to about 0.3 % shear strain, the responses are more or less identical, but beyond that the hardening behaviours become somewhat different. All three cases, however, exhibit the same characteristic feature that the hardening rate decreases until the shear stress reaches a maximum. After that, the stress level drops to some extent before settling to a 'steady state' value corresponding to constant dislocation densities. This is particularly clear for case b. Thus, the simulations lead to the introduction of two characteristic strength levels:

the *yield strength* corresponding to the peak in the stress-strain curve, and the (lower) *flow strength* at which the material continues to deform steadily. It is interesting to note that the yield strengths and the corresponding yield strains depend on the initial relaxed dislocation structure, whereas the flow strengths for the three cases seem to be almost identical. As discussed above, 'flow' occurs by localized activity on a few slip planes which is largely controlled by the dislocation pile-ups. The breaking-away of the leading dislocation in such pile-ups plays a crucial role in the process. Thus, the flow strength in the simulations seems to be determined mainly by the density and strength of the obstacles.

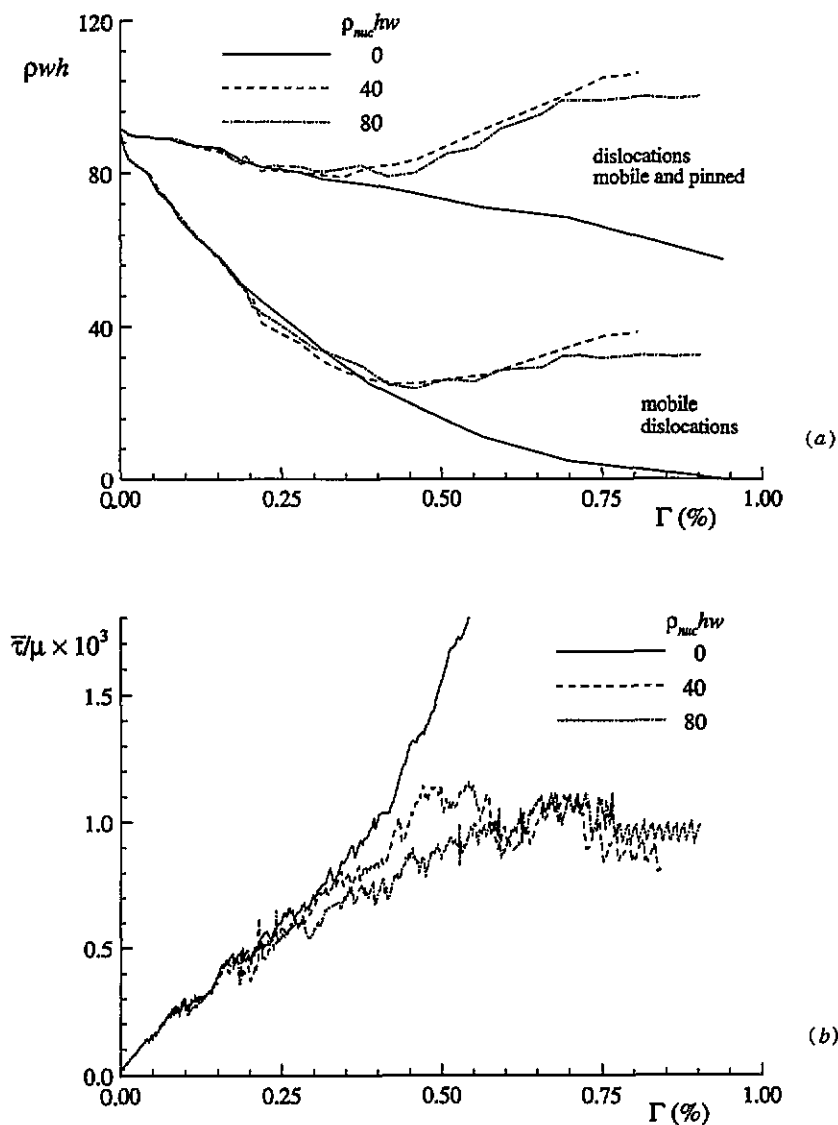


Figure 10. Effect of density of dislocation sources on the simple shear response. (a) Evolution of total and mobile dislocation densities, (b) overall shear stress response.

5.3. Influence of source and obstacle density

In the above-mentioned computations, the behaviour was seen to be controlled primarily by the rate of nucleation of new dislocations and the rate of annihilation. The purpose of this section is to study how these depend on the densities of obstacles and sources in the present type of simulations. In doing so, we shall be comparing with the case shown in figures 6 to 9, for which the densities are $\rho_{\text{nuc}} = 80/hw$ and $\rho_{\text{obs}} = 160/hw$.

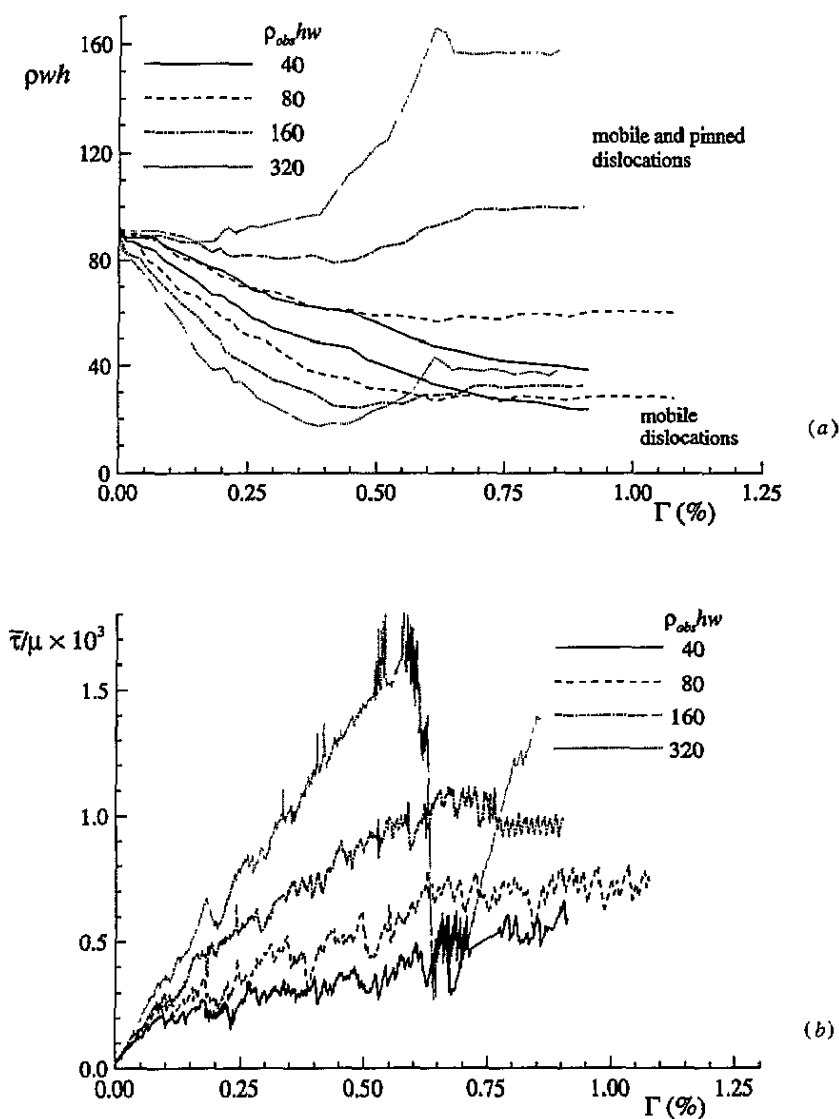


Figure 11. Effect of obstacle density. (a) Evolution of total and mobile dislocation densities, (b) overall shear stress response.

Figure 10 shows some results when the source density is halved (by randomly taking out half of the sources) or, as a limiting situation, when there are no active dislocation sources.

From the fact that the dislocation density is seen to be independent of the source density until $\Gamma \approx 0.25\%$, it is concluded that the simulated behaviour is essentially annihilation controlled. Beyond that strain level, all remaining dislocations tend to be removed by annihilation if there are no sources, figure 10(a), and the response would tend to become purely elastic, see figure 10(b). If there are sufficient sources, dislocation generation wins out over annihilation at some point. The rate of dislocation nucleation then appears to be virtually independent of the source density, and will be controlled by the strength of the sources. The corresponding stress-strain response shows the typical yield and subsequent flow characteristics, with the actual source density having some effect on the hardening behaviour and the yield strain, but being seemingly unimportant for the yield strength and for the flow strength.

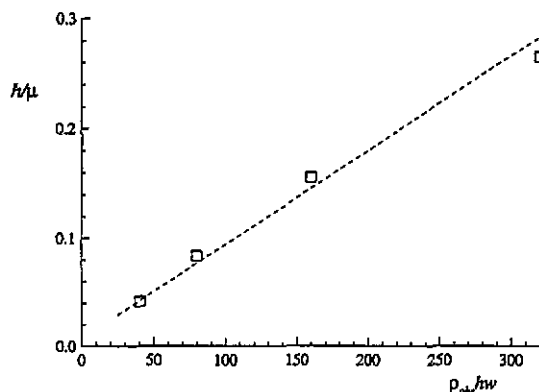


Figure 12. Average hardening modulus $h = d\bar{\tau}/d\Gamma$ from the stress-strain curves in figure 11 as a function of the corresponding obstacle density.

The effect of obstacle density is briefly studied in figure 11. Relative to the reference density $\rho_{\text{obs}} = 160/hw$, we consider half and quarter of that density (by randomly removing obstacles) and a case with twice as many obstacles (by adding obstacles). The initial dislocation distribution and the source distribution again correspond to case a in figures 6 to 9. The two cases with the lower obstacle density exhibit a more or less monotonic decrease of dislocation density until the steady-state value is reached. Correspondingly, the stress-strain responses do not show a distinct yield point, but a more gradual transition to flow. For the case with the highest density, $\rho_{\text{obs}} = 320/hw$, however, annihilation is essentially inactive. This is attributed to the fact that for the given initial (mobile) dislocation density of $\rho = 93/hw$, the obstacles effectively prevent dislocation motion over distances large enough for annihilation to become possible. As a consequence, there is relatively strong initial strain hardening, and a very sharp yield point, corresponding to a peak in the mobile dislocation density. The strain regime just after the stress drop is characterized by a very high annihilation-generation activity that continues until around $\Gamma = 0.7\%$, after which the dislocations seem to have found 'stable' positions, and the material hardens again. Notice, however, that on average the dislocation density remained constant after yield. The computation with $\rho_{\text{obs}} = 320/hw$ took over 300 000 increments due to the fact that the time steps needed to be small because of the extremely high nucleation-annihilation activity.

For each of the results in figure 11(b), we have fitted a linear hardening curve to the response prior to the yield point. For each obstacle density, the slope of this linear fit, $h = d\bar{\tau}/d\Gamma$, is plotted versus the corresponding obstacle densities in figure 12, and shows

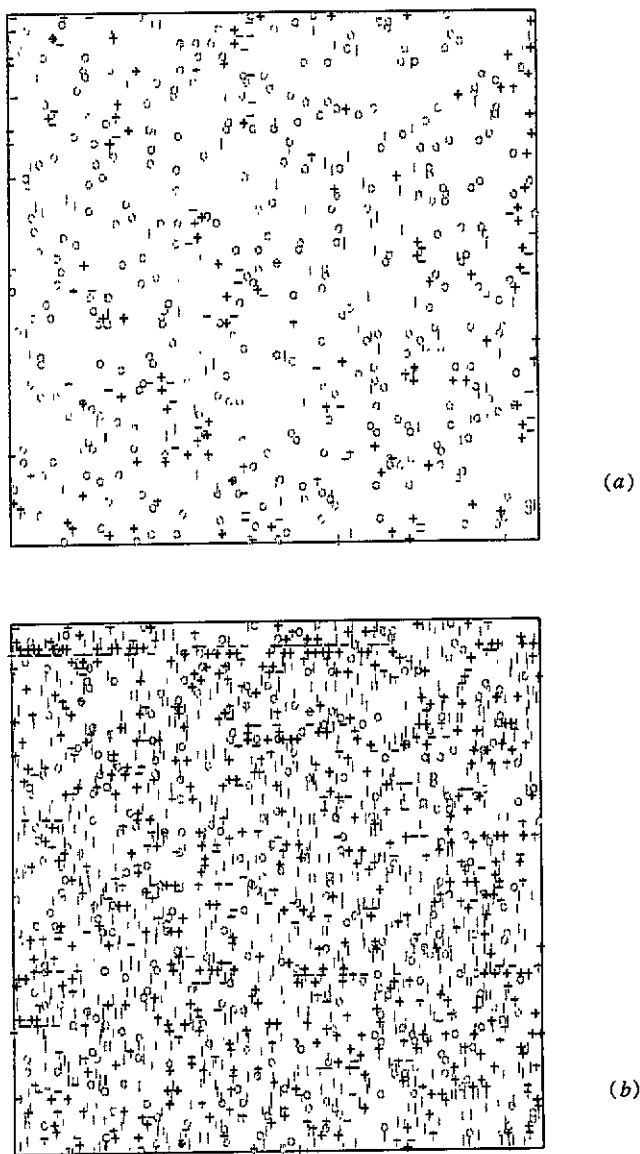


Figure 13. Dislocation distributions for different obstacle densities (see also figure 11): (a) $\rho_{\text{obs}} = 40/hw$ at $\Gamma = 0.87\%$, (b) $\rho_{\text{obs}} = 320/hw$ at $\Gamma = 0.86\%$.

a remarkably linear correlation between h and ρ_{obs} . Our explanation of this is as follows. As mentioned before, prior to yield, the process is controlled mainly by annihilation. Dislocations in those stages are still distributed relatively diffusely and the obstacles then mainly act to decrease the probability of annihilation by pinning dislocations. Thus, the rate of annihilation decreases with increasing obstacle density, and therefore the hardening modulus h in the present simulations increases with increasing obstacle density.

Figure 13 shows dislocation distributions at about the same strain levels for the two extreme obstacle densities, $\rho_{\text{obs}} = 40/hw$ and $\rho_{\text{obs}} = 320/hw$. Notice that for the lower obstacle density, no localization of slip activity takes place, which is consistent with the

absence of a yield point (see figure 11(a)).

5.4. Evolution of cell walls

The computations presented in sections 5.2 and 5.3 have started out from an initially random dislocation distribution. In this section, we present a few results for computations where the initial dislocations are organized in parallel walls of opposite dislocations, representing small-angle grain boundaries [20, 21]. In fact, we consider walls parallel to the x_2 direction and spaced at a distance w , so that our unit cell contains two walls, as shown in figure 14. We consider two cases: one where all dislocations in the walls are pinned and one where they are left free to move. In each of the two cases we then introduce the same random sources and obstacles, with densities $\rho_{\text{nuc}} = \rho_{\text{obs}} = 80/hw$.

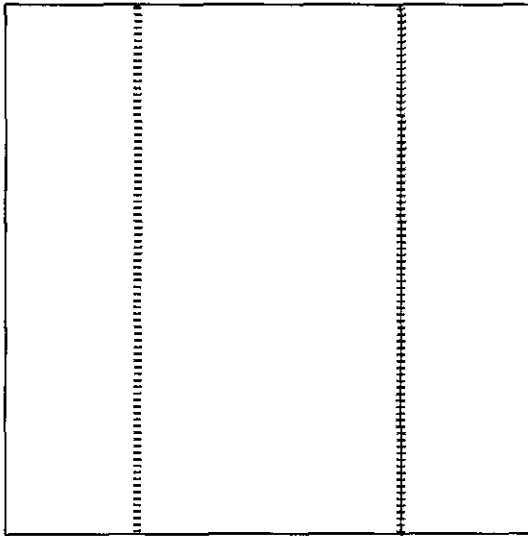


Figure 14. Unit cell containing two parallel dislocation walls at mutual distance w .

It is well-known (e.g. [20, 21]) and was confirmed in the computations in [8] that in the undeformed state, these dislocation walls are in stable equilibrium. Upon shearing however they cease to be so (as also seen in [8]). In the case of the free walls, they initially bow out, and then activate nearby dislocation sources. When the process continues, the wall structures are gradually dissolved, as is shown in figure 15(a). In the stress-strain curve, depicted in figure 16, this is reflected in a small amount of plasticity in the beginning of deformation, but yielding only takes place after $\Gamma \approx 0.13\%$. On the other hand, when all dislocations in the walls are pinned at obstacles, the walls mainly act to generate a nonuniform stress field, which determines where nucleation of new dislocations will occur. After nucleation is initiated, individual dislocations in the walls get removed by annihilation, as seen in figure 15(b), but eventually the process evolves into a steady-state situation with dislocation activity in a few slip planes as in figure 5. The stress-strain response for the pinned walls shows rather abrupt yielding (see figure 16). The yield strain is roughly the same as for the case with free dislocation walls, but the yield strength is considerably higher.

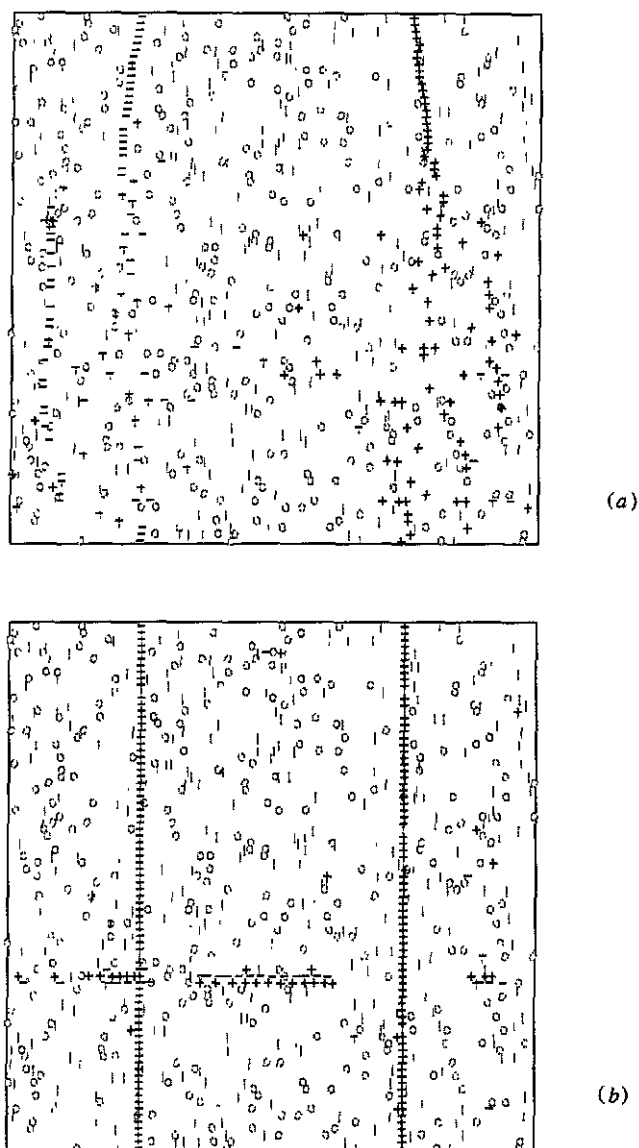


Figure 15. Dislocation distributions during simple shear for cases where the initial dislocations are organized in walls (see figure 14) and are either left free to move or are pinned. (a) free walls, $\Gamma = 0.36\%$, (b) pinned walls, $\Gamma = 0.35\%$.

6. Results for composites

In this section, results are presented for a material containing a periodic array of square particles ($w_f = h_f$ in figure 4). The loading conditions and properties of the matrix material are taken to be identical to those in section 5; the elastic properties of the inclusions are specified as $\nu^* = 0.17$ and $\mu^* = 7.3\mu$ (taking the matrix elastic constants to be representative for aluminium, the parameter values for the inclusion are indicative for the properties of silicon carbide).

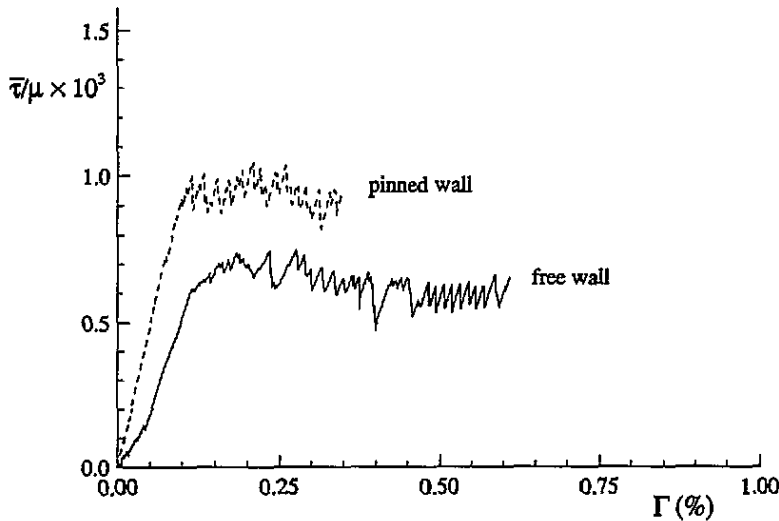


Figure 16. Overall shear stress response to simple shear for cases where the initial dislocations are organized in pinned or free dislocation walls (see figure 14).

Figures 17 and 18 show results for two materials with the same area fraction $f = (wh)/(w_f h_f) = 0.2$ but with different distributions of obstacles and sources. In the matrix region, the obstacle and source distribution in figure 17 is the same as that in figure 8(a), while the figure 18 distribution corresponds to figure 8(b) (cf. section 5). In both cases, the matrix is initially dislocation-free. For the case shown in figure 17, plastic deformation tends to concentrate in the layer of matrix material in between the rows of inclusions; there is no dislocation activity on slip planes between inclusions. In fact, as is clear from figure 17(b), the dislocation density is still at a low level when all dislocation activity takes place within a narrow band of a few slip planes, similar to what was found in many of the simulations for homogeneous material in section 5. Figure 18, for a different source and obstacle distribution, shows a somewhat different behaviour, where the first dislocations appear almost exclusively in the layers between rows of inclusions (figures 18(a) and (b)), but where at a later stage in the deformation dislocations are also generated in between inclusions, as seen in figure 18(c). Finally, again, localization of dislocation activity on a few slip planes occurs.

Figure 19 shows results for a material with smaller inclusions, $f = 0.05$. The source and obstacle distributions in the matrix material are taken to be the same as in figure 8(b) and figure 18. As in figure 18, slip band formation occurs (see figure 19(b)).

Curves of overall composite shear stress versus shear strain are shown in figures 20(a) and (b). Figure 20(a) shows comparisons with continuum slip predictions for $f = 0.20$. In the continuum slip formulation the hardening behaviour is an input to the analysis and not an outcome as it is for the dislocation based plasticity calculations. The values of N and γ_0 for use in (32) were chosen to fit the initial plastic hardening behaviour found for the two cases in figures 17 and 18 and the value of m in (33) was taken as 0.005 to give nearly rate-independent response. Since the continuum slip strain hardening behaviour is specified to be monotonic, the stress drop of the dislocation based analyses is not represented. (If a strain softening relation were assumed in the continuum analysis instead of the hardening law (32), shear band localization would occur.)

Figure 20(b) shows the effect of reinforcement area fraction f . The composite elastic

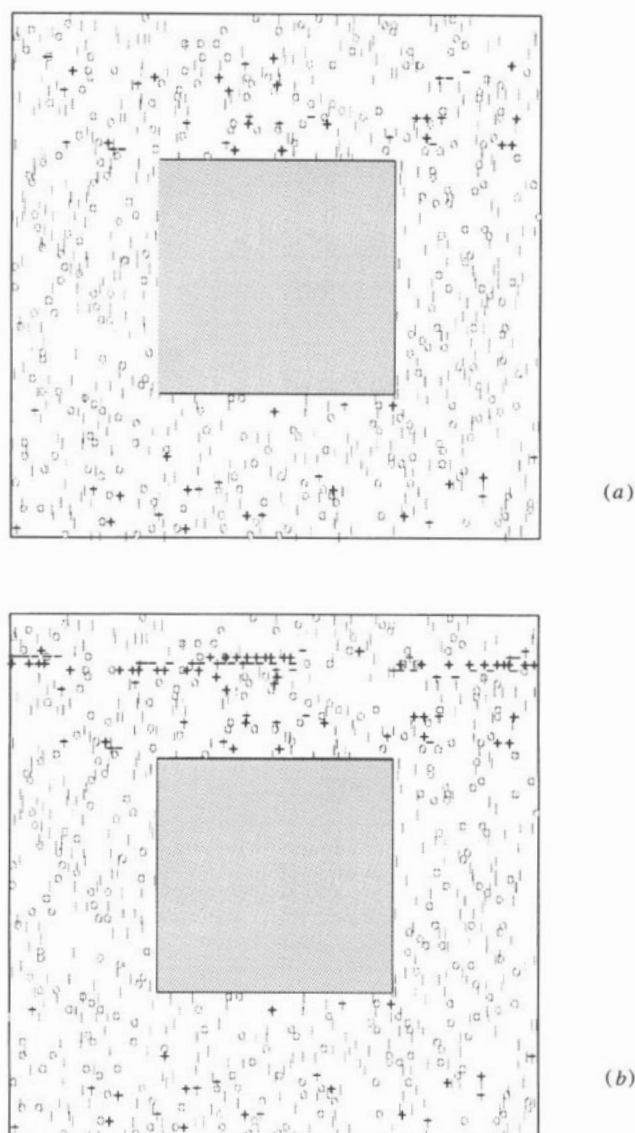


Figure 17. Dislocation distributions in an initially dislocation-free material with an area fraction $f = 0.2$ of elastic inclusions. The distribution of sources and obstacles is the same as in figure 8(a). (a) $\Gamma = 0.19\%$, (b) $\Gamma = 0.44\%$.

modulus and the initial hardening depend on f , but the flow strength does not. This is expected since the flow strength is associated with the localization of dislocation activity in the matrix and mainly depends on the density and strength of matrix obstacles (cf. Section 5.2). As for other cases where slip band formation is observed, the stress-strain curve exhibits a distinct yield point and continued plastic flow at a lower stress level. The case shown in figure 18, however, where there is a relatively high, diffuse dislocation activity, exhibits a prolonged period of strain hardening before localization in few slip planes occurs at around $\Gamma = 0.7\%$. The flow strength levels are approximately the same for all three

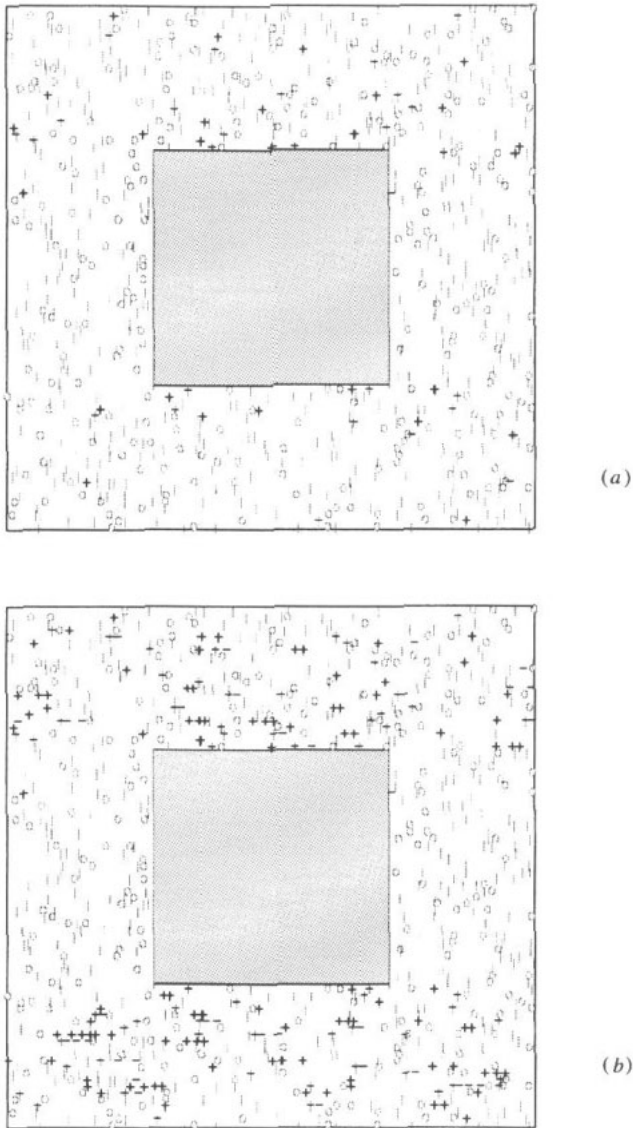


Figure 18. Dislocation distributions in an initially dislocation-free material with an area fraction $f = 0.2$ of elastic inclusions. The distribution of sources and obstacles is the same as in figure 8(b). (a) $\Gamma = 0.19\%$, (b) $\Gamma = 0.48\%$, (c) $\Gamma = 0.78\%$.

dislocation-based calculations considered here. They also seem to have roughly the same flow strength values as for the unreinforced matrix material (see figure 9). This suggests that the inclusions affect the generation and motion of dislocations through the inhomogeneous stress fields generated in the matrix, but that they do not directly influence the localization of dislocation activity itself. This is expected because the reinforcement does not block all the slip planes, as noted in a phenomenological plasticity context by Drucker [30].

The evolution of the mobile and total dislocation densities for the three dislocation based calculations in figures 20(a) and (b) is shown in figure 20(c). In each case, the material is

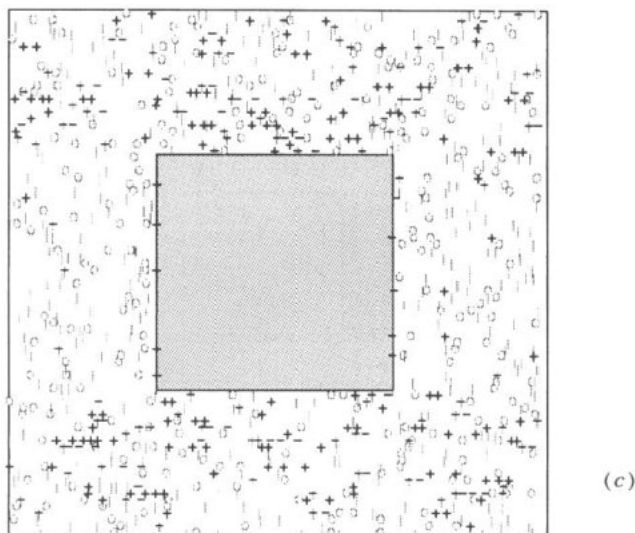


Figure 18. (Continued)

initially dislocation free and remains so until the stress level is high enough for the weakest source to be activated. Most of the nucleated dislocations become pinned so that the mobile dislocation density is much less than the total dislocation density. When the dislocation activity localizes on a few slip planes, a rather constant dislocation density is maintained as for the monophase material in figure 7.

Figure 21 shows the distribution of the total shear stress σ_{12} calculated from (1), normalized by the overall shear stress $\bar{\tau}$ for the case shown in figure 18 at four stages of deformation. The lowest contour in figure 21 corresponds to $\sigma_{12} = 0$, so that within the region enclosed by this contour σ_{12} has the opposite sign of the overall shear stress. The stage shown in figure 21(a) is when only two dislocations, in the lower right hand corner of the unit cell, have been nucleated. The long-range effect of the dislocation stress fields is seen in this figure. Even though there is little dislocation patterning noticeable, the stresses away from the dislocation cores can easily become several factors higher than the average shear stress.

The stress fields obtained from the dislocation-based and the continuum slip plasticity calculations are compared in figures 22 to 25. Figure 22 compares the shear stress distribution for the rather high hardening case in figure 18 with that from the continuum slip calculation using $N = 0.3$ at $\Gamma \approx 0.5\%$. Since the shear stress distribution in the discrete dislocation calculation is dominated by the discrete dislocation fields, the shear stress distributions are entirely different. In particular, because of the long range dislocation stress fields, the shear stress distributions in the reinforcement from the two calculations differ substantially. The shear stress distributions from the case in figure 17 and from the continuum slip calculation with $N = 0.1$ are shown in figure 23, also at $\Gamma \approx 0.5\%$. The stage shown in figure 23(a) is after dislocation activity has localized on a few slip planes and the dislocation density has reached its steady-state value. As in figure 22 regions in the reinforcement in figure 23(a) have significantly higher shear stress than is given by the continuum slip distribution in figure 23(b). In both figure 23(a) and figure 23(b), there is a relatively low value of the shear stress in the matrix alongside the reinforcement.

Figures 24(a) and 25(a) are for the case from figure 18 at $\Gamma = 0.78\%$, which is after the

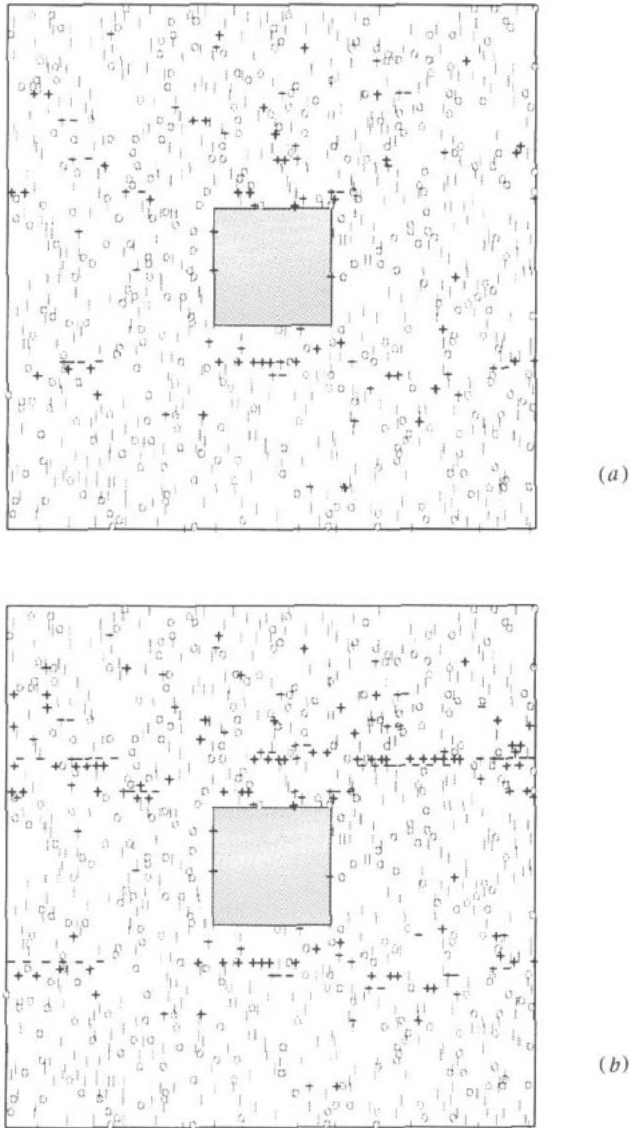


Figure 19. Dislocation distributions in an initially dislocation-free material with an area fraction $f = 0.05$ of elastic inclusions. The distribution of sources and obstacles is the same as in figure 8(b). (a) $\Gamma = 0.26\%$, (b) $\Gamma = 0.66\%$.

stress drop due to the localization of dislocation activity on a few slip planes has occurred. The shear stress distribution is shown in figure 24 and the sum of the in-plane normal stresses, $\sigma_{\alpha\alpha} = \sigma_{11} + \sigma_{22}$ is shown in figure 25. The continuum slip solutions shown are for the $N = 0.1$ calculation at a comparable strain. However, the stress histories are different since there is no stress drop in the continuum slip analysis. Again, the stress distributions in figures 24(a) and 25(a) are dominated by the discrete dislocation fields and the stress magnitudes in the reinforcement are greater than given by the continuum slip analyses in figures 24(b) and 25(b). The value of $\sigma_{\alpha\alpha}$ scales with the actual mean stress (apart from a

correction that would have to be applied inside the inclusion due to the polarization stress in (6)), and is seen to be distributed in a rather patchy manner with relatively extended regions of high positive values and regions of high negative values. In particular, it is interesting to note the regions of high tensile mean stresses near the lower left-hand and upper right-hand corners of the reinforcement. In figure 25(a), the strong effects of the discrete dislocation fields dominate over the effect of the stress concentration at the reinforcement corners seen in figure 25(b).

It is evident from figures 22 to 25 that the stress fields obtained from the discrete dislocation calculations differ substantially from their continuum slip counterparts. However, in making the comparison, one should realize that the continuum slip formulation implies averaging of fields over many dislocations in the material element, while the dislocation densities in the computations presented here are still rather low (of the order of 10^9 cm^{-2} for $h = w = 1 \text{ }\mu\text{m}$).

7. Concluding remarks

A continuum mechanics based approach for analysing microscale plastic flow processes has been presented where plastic flow arises directly from the collective motion of large numbers of dislocations. The formulation consists of: (i) accounting for the long-range interaction between dislocations by considering the dislocations as singularities in an infinite elastic medium (for which analytical expressions are available in a number of cases of interest); (ii) representing other interactions between dislocations or characteristics of dislocation motion, such as dislocation nucleation and annihilation, and dislocation drag, through a set of constitutive rules; and (iii) obtaining the correction (or image) fields that are needed to meet the boundary conditions, on the basis of the numerical solution to a standard linear elastic boundary value problem. The present computational framework permits rather general initial/boundary value problems to be formulated and solved for dislocated solids.

To demonstrate some of the features of the approach, the formulation has been implemented for two-dimensional plane strain problems for solids having edge dislocations on parallel slip planes. Even in this simple case, there are aspects of the formulation that provide computational challenges. One is the computation of the long-range interactions. Here, for doubly periodic cells, the explicit summing of the contributions of long strings of dislocations (appendix C) provides an efficient procedure. In more general circumstances, the fast summation algorithm of Wang and LeSar [31] could be used. What proved to be the computational limiting factor in the calculations here however, was the small time step required. The time limiting factors were mainly (i) the short time scale associated with nucleation events and (ii) the numerical stability considerations associated with the strong dislocation interactions in pile-ups. Using parameters representative of fcc metals (like Al, Cu), up to 300 000 time steps were required for an imposed strain of about 1%.

Computations have been presented for monophase and composite materials with periodic microstructures subjected to simple shear loading. Even though they are only for a single slip system and use simple assumptions for sources and obstacles, the results show a number of noteworthy features. Equilibrium dislocation configurations exhibit a tendency to form organized patterns, as in figure 6 (see also [1, 3, 6, 8]), but the organized pattern breaks down under an applied (monotonic) stress. This is even so for perfect wall structures, figure 15.

Upon continued monotonic deformation, and with random distributions of obstacles and sources, the results show no evidence of a tendency for spatial patterning, even though

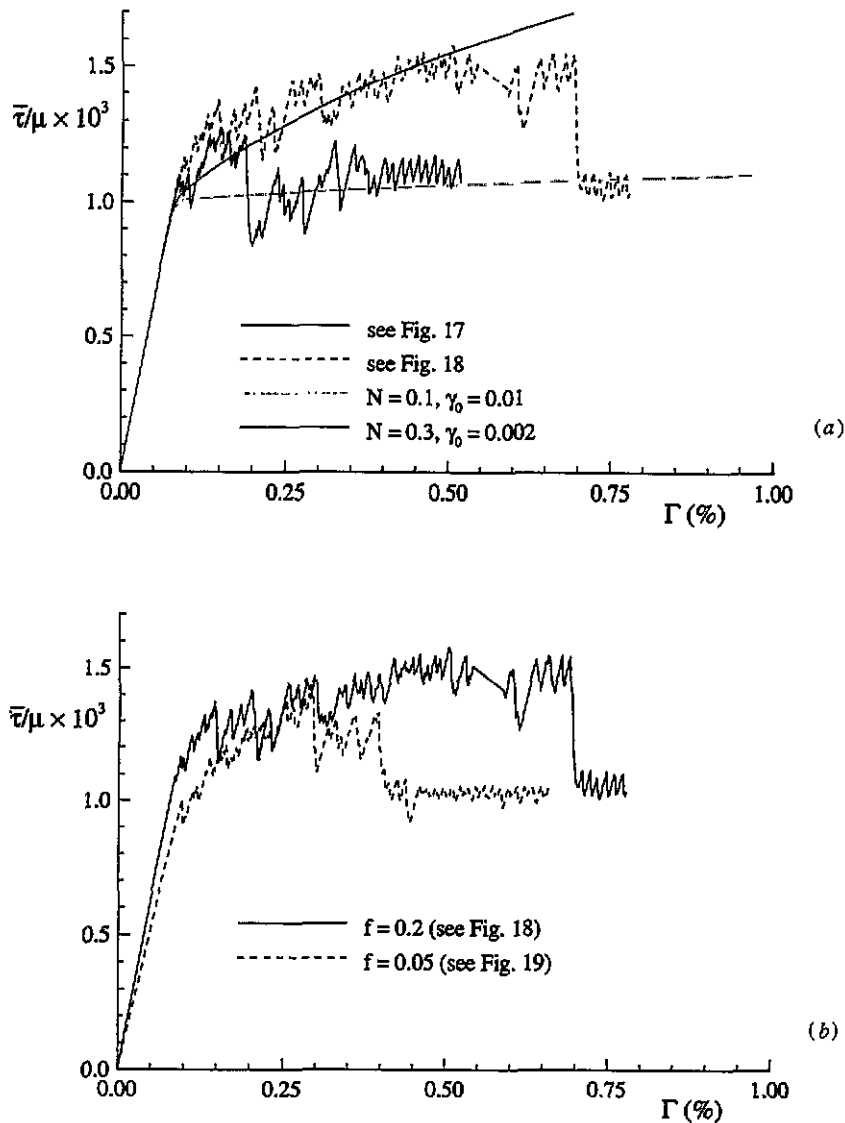


Figure 20. Overall response to simple shear corresponding to the cases shown in figures 17–19. Shear stress responses are shown in (a) and (b), in comparison with continuum slip results based on two sets of hardening parameters N , γ_0 . The evolution of dislocation densities is plotted in (c).

that was one of the driving forces for the development of discrete dislocation plasticity approaches. It may be that dislocation patterning, when it is observed experimentally, occurs in regions that are relatively obstacle-free or where the prior deformation history has greatly decreased the density of obstacles (for instance, due to cyclic loading). Here, instead, the dislocation activity is found to localize in a small number of slip planes, determined by the (stochastic) spatial distribution of sources and obstacles. This kind of localization of slip activity in such 'planar arrays' has also been found for instance in simulations by Amodeo and Ghoniem [3] and is suggestive of the coarse slip lines or coarse slip bands

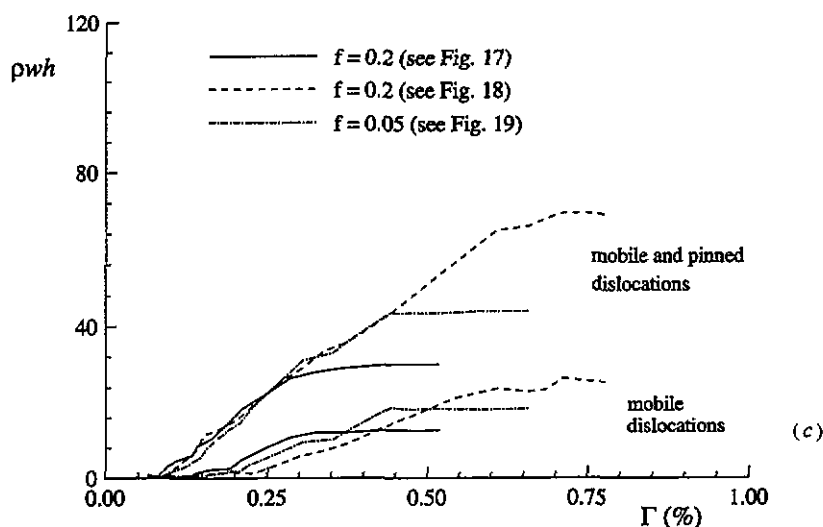


Figure 20. (Continued)

which are often observed in crystalline metals (see, e.g., [25]).

Related to this type of behaviour is the occurrence of two characteristic strength levels in the simulations: a yield strength, corresponding to a local peak in the stress-strain response, and a flow strength, at which the material deforms at a more or less constant shear stress level. This flow strength is associated with the more or less 'steady-state' state dislocation pattern after localization of the slip activity. In the dependence of these strength levels on the sources and obstacles assumed in the computations, there seems to be a rather sharp transition from source-limited plasticity to obstacle controlled plasticity. At a sufficiently low source density, the dislocation process is completely source-limited; above a certain source density however, the mentioned typical response is observed with the pre-yield as well as post-yield behaviour being controlled by the obstacle density and the strength of the obstacles.

The computations have been carried out for a highly idealized model problem. A substantial part of any lack of correspondence with real material behaviour must, of course, be attributed to some of the highly simplifying assumptions made in the constitutive rules used in these initial calculations. There are several obvious improvements. One key extension seems to be to account for dislocation motion on more than one slip system. This will immediately involve the dynamic formation of obstacles (in the form of forest dislocations) and sources due to multiple slip. It is emphasized that the formulation of the technique immediately allows for this; it only involves a small extension of the set of constitutive rules. Also, in order to provide a quantitative description of real material behaviour, the computational implementation has to be extended to three-dimensional geometries.

There is a great deal of interest in problems of, for instance, plastic flow near crack tips, around micro-indentors and in composite materials, at a size scale where the collective motion of large numbers of dislocations and discrete dislocation effects play a role. The results presented in section 6 on composite materials are a reminder of the averaging procedures that underlie continuum plasticity descriptions. They indicate that for the aforementioned microscale problems, continuum plasticity may not give the desired resolution of stress and strain fields on that scale, and that the discrete nature of dislocations

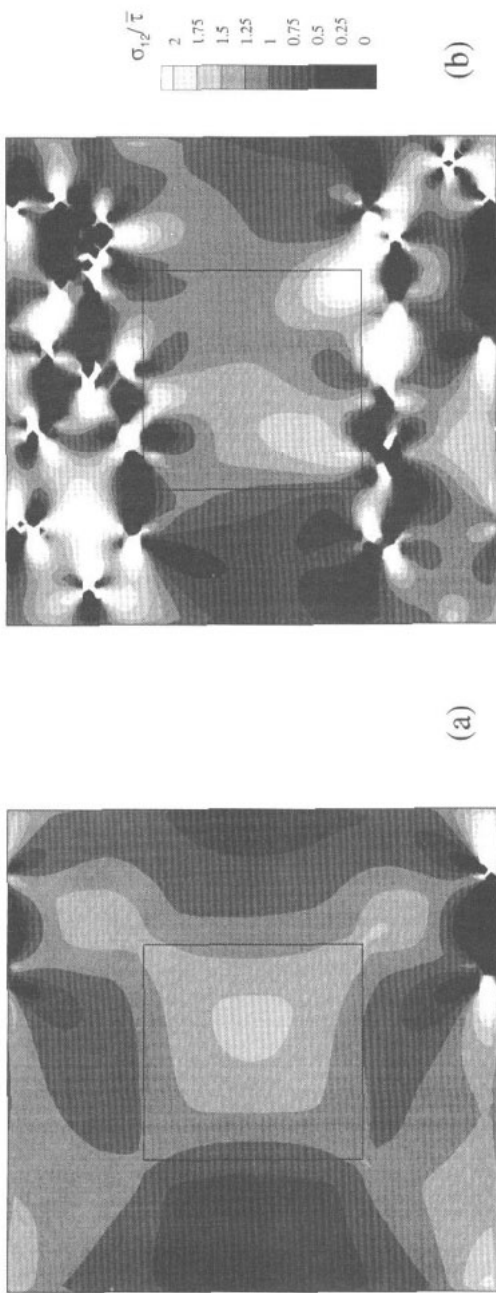


Figure 21. Shear stress distributions, normalized by the ov rail shear stress $\bar{\tau}$, for the case shown in figure 18. (a) $\Gamma = 0.087\%$ (b) $\Gamma = 0.14\%$ (c) $\Gamma = 0.48\%$ (d) $\Gamma = 0.78\%$.

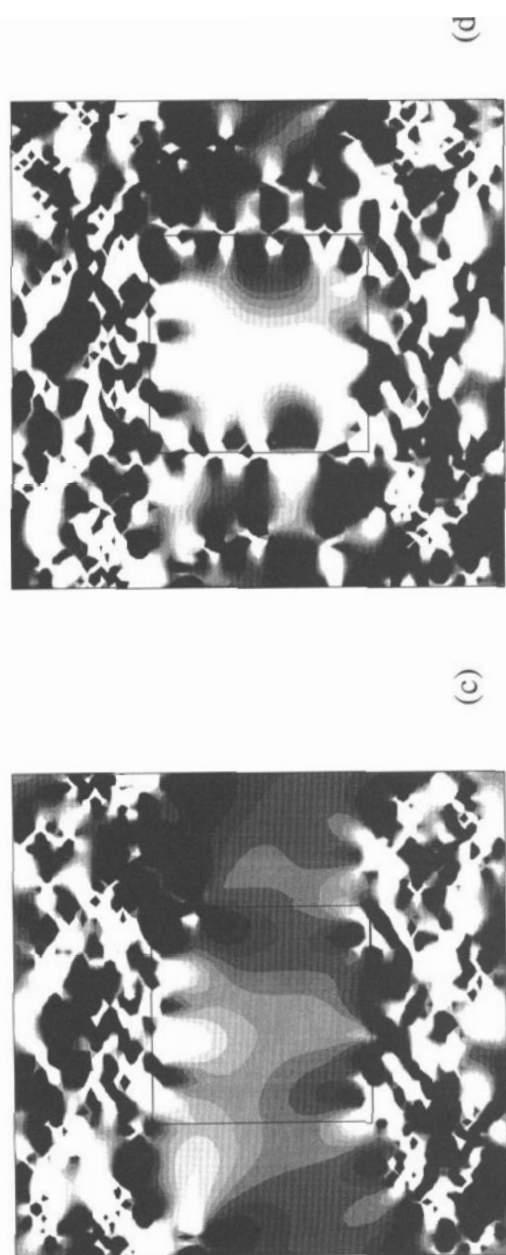


Figure 21. (C nined)

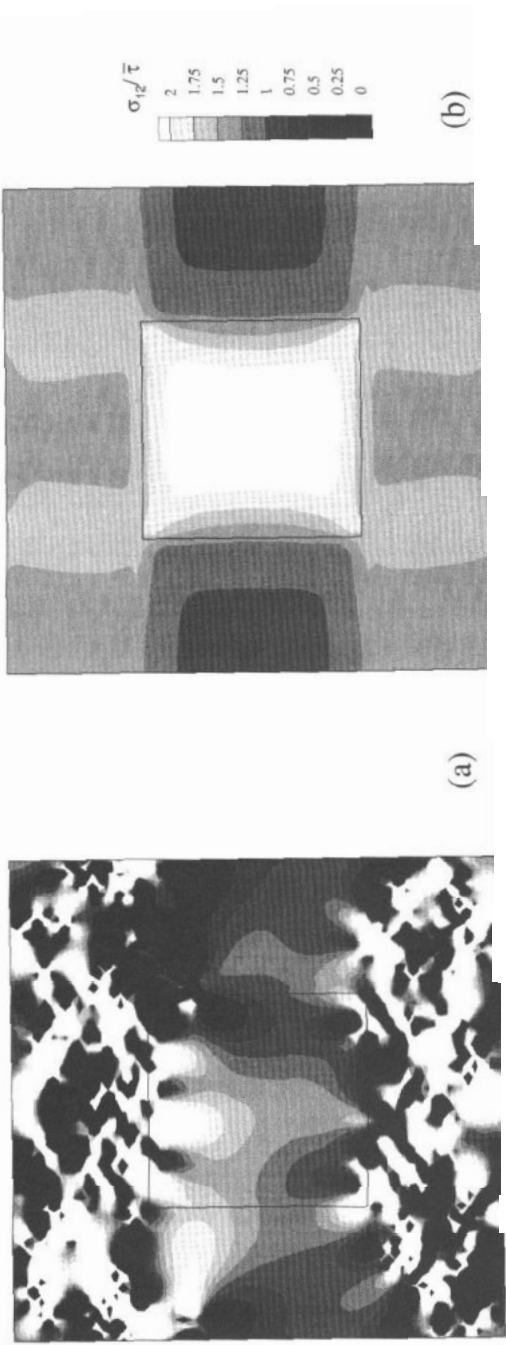


Figure 22. Shear stress distributions, normalized by the overall shear stress $\bar{\tau}$, for (a) the case shown in figure 18(b) at $\Gamma = 0.48\%$ and (b) for the continuum slip computation with $N = 0.3$, $\eta_1 = 0.002$ at $\Gamma = 0.50\%$ (cf. figure 20(i)).

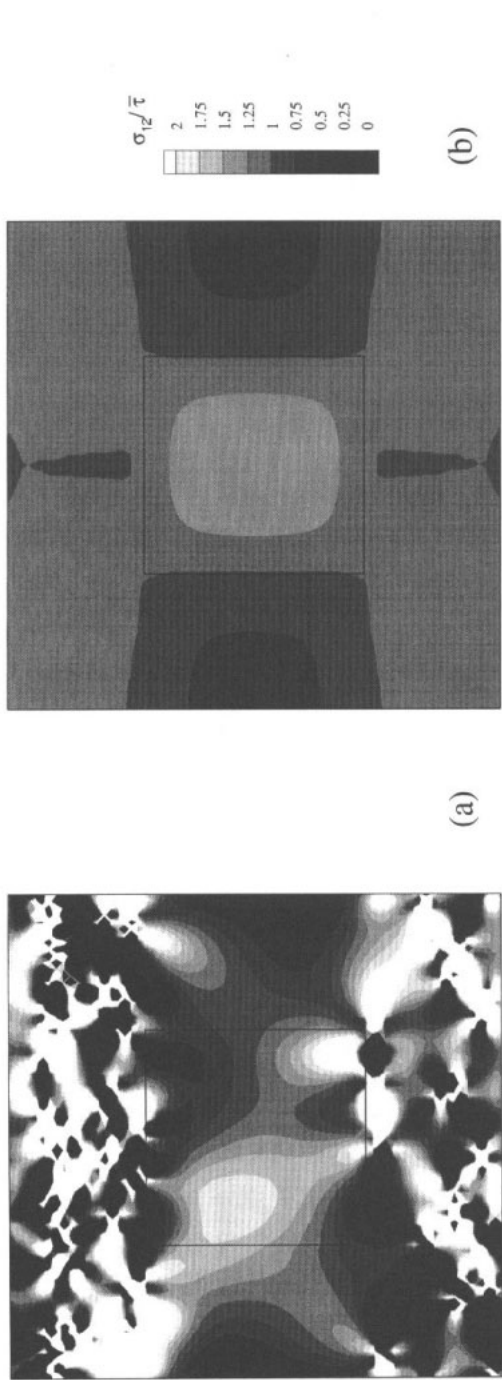


Figure 23. Shear stress distributions, normalized by the overall shear stress $\bar{\tau}$, for (a) the case shown in figure 17(b) at $\Gamma = 0.52\%$, and (b) for the continuum slip computation with $N = 0.1$, $y_0 = 0.01$ at $\Gamma = 0.49\%$ (cf. figure 20(a)).

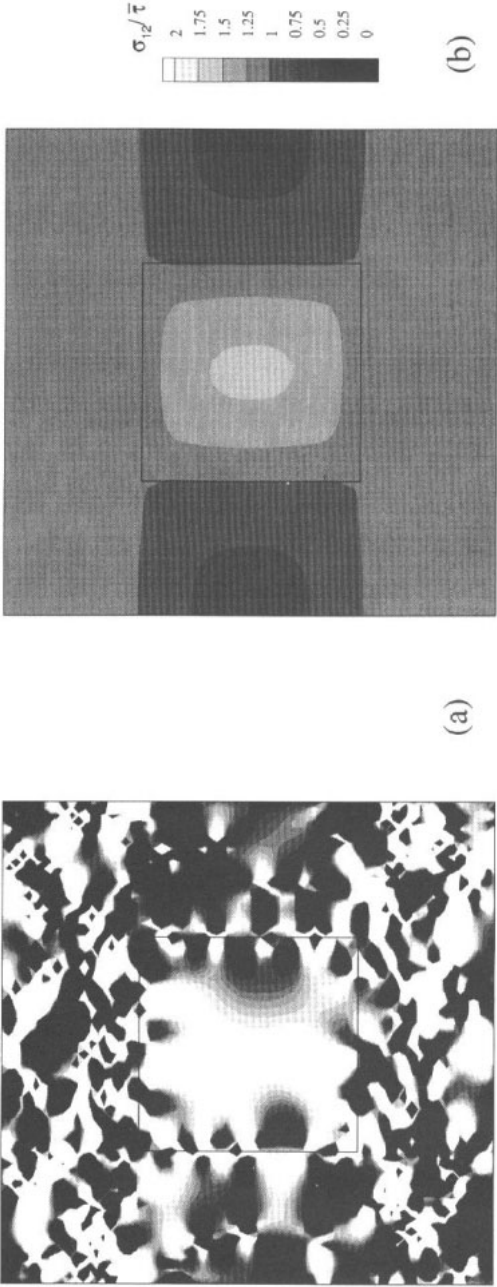


Figure 24. Shear stress distributions, normalized by the overall shear stress $\bar{\tau}$, at $\Gamma = 0.78\%$ for (a) the continuum slip computation with $N = 0.1$, $\gamma_0 = 0.01$, and (b) for the

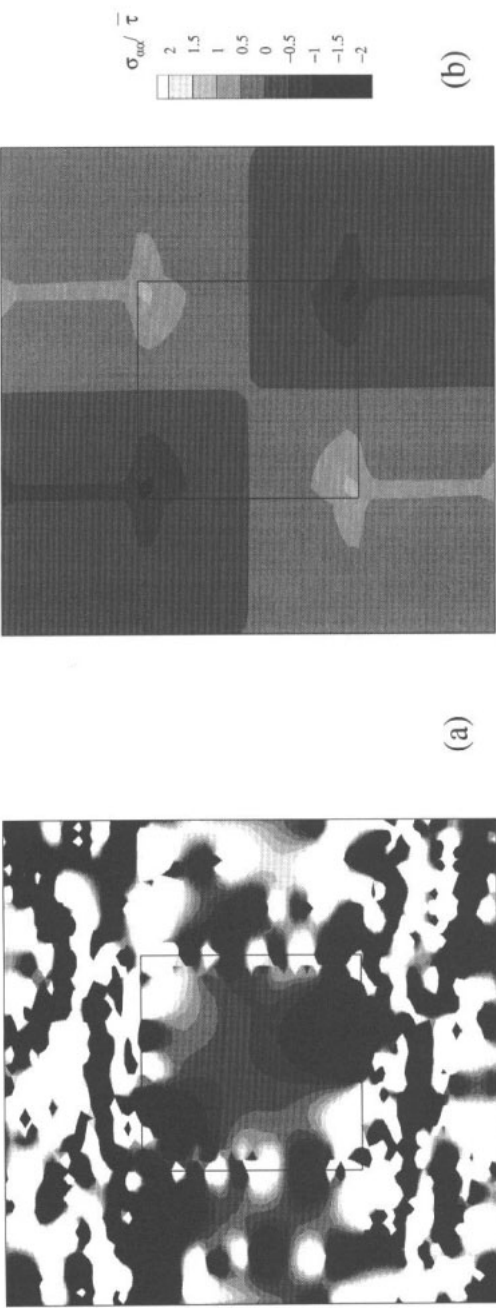


Figure 25. Distributions of the 'mean stress' σ_{eq} , normalized by the overall shear stress $\bar{\tau}$ at $\Gamma = 0.78\%$ for (a) the state shown in figure 18(c), and (b) for the continuum slip computation with $N = 0.1$, $\gamma_0 = 0.01$.

may need to be accounted for. The general formulation here provides a framework to address such problems. Even in a two-dimensional plane strain context, substantial computational resources are required, but such computations are currently feasible.

Acknowledgments

We are pleased to acknowledge use of the workstation clusters at the Pittsburgh Supercomputer Center. Some of this work was carried out while E van der Giessen was visiting at Brown University; this visit was made possible by financial support from the Netherlands Technology Foundation STW. A Needleman is grateful for support from the Materials Research Group on *Micro- and Nano-Mechanics of Failure-Resistant Materials*, funded at Brown University under NSF Grant DMR-9223683, and from the Air Force Office of Scientific Research under grant F49620-94-1-0300.

Appendix A. Derivation of (10)

We start by writing the potential energy for the volume \hat{V} excluding the core regions around all dislocations as

$$\Pi = \frac{1}{2} \int_{\hat{V}} \boldsymbol{\sigma} : \boldsymbol{\epsilon} \, dV - \frac{1}{2} \int_{\partial \hat{C}} (-\mathbf{T}) \cdot \mathbf{u} \, dS - \int_{S_f} \mathbf{T}_0 \cdot \mathbf{u} \, dS$$

where the second term accounts for the core strain energies through the work of the tractions $-\mathbf{T}$ on the internal surfaces $\partial \hat{C}$ of \hat{V} (see figure 1(b)). After substitution of the decomposition in (1), one arrives at

$$\begin{aligned} \Pi = & \frac{1}{2} \int_{\hat{V}} \hat{\boldsymbol{\sigma}} : \hat{\boldsymbol{\epsilon}} \, dV + \frac{1}{2} \int_{\hat{V}} (\hat{\boldsymbol{\sigma}} : \tilde{\boldsymbol{\epsilon}} + \tilde{\boldsymbol{\sigma}} : \hat{\boldsymbol{\epsilon}}) \, dV + \frac{1}{2} \int_{\hat{V}} \tilde{\boldsymbol{\sigma}} : \tilde{\boldsymbol{\epsilon}} \, dV \\ & + \frac{1}{2} \int_{\partial \hat{C}} (\hat{\mathbf{T}} \cdot \hat{\mathbf{u}} + \hat{\mathbf{T}} \cdot \tilde{\mathbf{u}} + \tilde{\mathbf{T}} \cdot \hat{\mathbf{u}} + \tilde{\mathbf{T}} \cdot \tilde{\mathbf{u}}) \, dS - \int_{S_f} \mathbf{T}_0 \cdot (\hat{\mathbf{u}} + \tilde{\mathbf{u}}) \, dS. \quad (\text{A1}) \end{aligned}$$

The terms with (mixed) strain energies can, for example, be rewritten as

$$\int_{\hat{V}} \tilde{\boldsymbol{\sigma}} : \hat{\boldsymbol{\epsilon}} \, dV = \int_{\hat{V}} \tilde{\boldsymbol{\sigma}} : \hat{\boldsymbol{\epsilon}} \, dV - \int_{\hat{C}} \tilde{\boldsymbol{\sigma}} : \hat{\boldsymbol{\epsilon}} \, dV = \int_{\hat{V}} \tilde{\boldsymbol{\sigma}} : \hat{\boldsymbol{\epsilon}} \, dV - \int_{\partial \hat{C}} \tilde{\mathbf{T}} \cdot \hat{\mathbf{u}} \, dS$$

where use has been made of the fact that the singularities in the infinite-medium dislocation stress fields $\tilde{\boldsymbol{\sigma}}$ are weak enough to allow for application of the divergence theorem and the equilibrium conditions in (3), provided that $\hat{\mathbf{u}}$ is smooth on \hat{C} . Strain energy terms with $\hat{\boldsymbol{\sigma}} : \tilde{\boldsymbol{\epsilon}}$ or $\tilde{\boldsymbol{\sigma}} : \hat{\boldsymbol{\epsilon}}$ can be worked similarly. Upon substitution of (2), the terms with $\tilde{\boldsymbol{\sigma}} : \tilde{\boldsymbol{\epsilon}}$ are expanded as

$$\begin{aligned} \int_{\hat{V}} \tilde{\boldsymbol{\sigma}} : \hat{\boldsymbol{\epsilon}} \, dV &= \sum_j \sum_k \int_{\hat{V}} \sigma^j : \epsilon^k \, dV = \sum_j \sum_k \int_{\hat{V}} \sigma^j : \epsilon^k \, dV - \sum_j \sum_k \int_{\hat{C}} \sigma^j : \epsilon^k \, dV \\ &= \sum_{j \neq k} \sum \int_{\hat{V}} \sigma^j : \epsilon^k \, dV + \sum_i \int_{\hat{V}} \sigma^i : \epsilon^i \, dV - \sum_i \sum_j \sum_k \int_{C^i} \sigma^j : \epsilon^k \, dV. \end{aligned}$$

The work of tractions associated with the infinite-medium fields is rewritten as

$$\begin{aligned}
 \int_{\partial \tilde{C}} \tilde{T} \cdot \tilde{u} \, dS &= \sum_i \sum_j \sum_k \int_{\partial C^i} T^j \cdot u^k \, dS \\
 &= \sum_i \int_{\partial C^i} T^i \cdot u^i \, dS + \sum_{i \neq j \neq k} \int_{\partial C^i} T^j \cdot u^k \, dS \\
 &= \sum_i \int_{\partial C^i} T^i \cdot u^i \, dS + \sum_{i \neq j \neq k} \int_{C^i} \sigma^j : \epsilon^k \, dV.
 \end{aligned}$$

Then, by substitution into (A1) and by noting that

$$\begin{aligned}
 \sum_i \int_V \sigma^i : \epsilon^i \, dV + \sum_{i \neq j \neq k} \int_{C^i} \sigma^j : \epsilon^k \, dV - \sum_i \sum_j \sum_k \int_{C^i} \sigma^j : \epsilon^k \, dV \\
 = \sum_i \int_{\hat{V}^i} \sigma^i : \epsilon^i \, dV
 \end{aligned}$$

one arrives at the expression (10).

Appendix B. Derivation of (11)

The derivation of (11) is to a large extent similar to the derivation given in [8], but special care should be taken here of the potential energy contribution of the inclusion. We start out with a straightforward variation of the expression (10) for the potential energy Π . Splitting up the first two integrals over matrix volume and inclusion volume, respectively, and insertion of the stress-strain relationships for (\cdot) as well as (\cdot) fields from (3) and (6), respectively, gives after some re-organization that

$$\delta \left\{ \frac{1}{2} \int_V \hat{\sigma} : \hat{\epsilon} \, dV + \frac{1}{2} \int_V (\hat{\sigma} : \tilde{\epsilon} + \tilde{\sigma} : \hat{\epsilon}) \, dV \right\} = \int_V \hat{\sigma} : \delta \hat{\epsilon} \, dV + \int_V (\hat{\sigma} : \delta \tilde{\epsilon} + \tilde{\sigma} : \delta \hat{\epsilon}) \, dV.$$

In order to determine the variation in the self-energy of each dislocation, we introduce the unbounded region E^i exterior to the small core volume C^i for the i th dislocation, and similarly the exterior \bar{V} of the body V . Then

$$\begin{aligned}
 \delta \left\{ \frac{1}{2} \int_{\hat{V}^i} \sigma^i : \epsilon^i \, dV + \frac{1}{2} \int_{\partial C^i} T^i \cdot u^i \, dV \right\} \\
 = \delta \left\{ \frac{1}{2} \int_{E^i} \sigma^i : \epsilon^i \, dV - \frac{1}{2} \int_{\bar{V}} \sigma^i : \epsilon^i \, dV + \frac{1}{2} \int_{\partial C^i} T^i \cdot u^i \, dV \right\} \\
 = - \int_{\bar{V}} \sigma^i : \delta \epsilon^i \, dV
 \end{aligned}$$

where in the last equality use is made of the fact that, under certain restrictions, the integrals over E^i and over ∂C^i remain invariant with respect to variations of the position of the dislocation. This invariance holds in all cases when the matrix material containing the

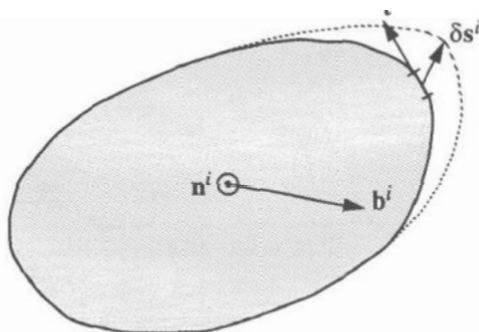


Figure B1. Cross-section along a slip plane, showing the change of the area S^i swept by dislocation i due to a variation δs^i of the position along the dislocation line. The normal vector to the slip plane, n^i , is pointing upwards out of the paper.

dislocation is isotropic. If the material is anisotropic, the variations δs^i must preserve the orientation of the slip plane relative to the directions of anisotropy.

The variation in potential energy is now obtained as

$$\delta \Pi = \int_V \hat{\sigma} : \delta \hat{\epsilon} \, dV + \int_V (\hat{\sigma} : \delta \tilde{\epsilon} + \tilde{\sigma} : \delta \hat{\epsilon}) \, dV + \sum_{j \neq k} \int_V \sigma^j : \delta \epsilon^k \, dV - \sum_i \int_{\hat{V}} \sigma^i : \delta \epsilon^i \, dV - \int_{S_j} T_0 \cdot (\delta \hat{u} + \delta \tilde{u}) \, dS. \quad (\text{B1})$$

The derivation proceeds by making use of the divergence theorem and the equilibrium conditions for the stress fields involved cf. (3) to (5). Subsequently,

$$\int_V \hat{\sigma} : \delta \hat{\epsilon} \, dV = \int_S \hat{T} \cdot \delta \hat{u} \, dS \quad (\text{B2})$$

$$\int_V \tilde{\sigma} : \delta \hat{\epsilon} \, dV = \int_S \tilde{T} \cdot \delta \hat{u} \, dS \quad (\text{B3})$$

$$\int_{\hat{V}} \sigma^i : \delta \epsilon^i \, dV = - \int_S T^i \cdot \delta u^i \, dS. \quad (\text{B4})$$

The volume integral with $\hat{\sigma} : \delta \tilde{\epsilon}$ needs special care in view of the fact that the singularities in $\tilde{\epsilon}$ vary in position when the positions, δs^i , of the dislocations are varied. We therefore again decompose the volume V into \hat{V} and the total excluded core region \bar{C} (see figure 1). Then

$$\int_V \hat{\sigma} : \delta \hat{\epsilon} \, dV = \int_{\hat{V}} \hat{\sigma} : \delta \hat{\epsilon} \, dV \quad (\text{B5})$$

since the integral over \bar{C} vanishes as $S_+^i \rightarrow S_-^i$ ($i = 1, \dots, n$) and $r_0 \rightarrow 0$. For a similar reason, after application of the divergence theorem, the surface integral over $\partial \bar{C}$ vanishes. But, a variation δs^i leads to a variation δS^i of the surface enclosed by the dislocation loop

The infinite-body stress components $\sigma_{\alpha\beta}$ at x_α due to this string of dislocations are obtained by summation of the stress fields due to each dislocation j over all integers. With (C1) it follows from (15)–(17) that

$$\sigma_{11} = \frac{a}{d} \sum_{j=-\infty}^{+\infty} \frac{\eta[3(\xi+j)^2 + \eta^2]}{[(\xi+j)^2 + \eta^2]^2} \quad (C2)$$

$$\sigma_{22} = -\frac{a}{d} \sum_{j=-\infty}^{+\infty} \frac{\eta[(\xi+j)^2 - \eta^2]}{[(\xi+j)^2 + \eta^2]^2} \quad (C3)$$

$$\sigma_{12} = -\frac{a}{d} \sum_{j=-\infty}^{+\infty} \frac{(\xi+j)[(\xi+j)^2 - \eta^2]}{[(\xi+j)^2 + \eta^2]^2} \quad (C4)$$

where

$$\xi = X/d \quad \eta = Y/d$$

and where

$$a = \frac{\mu b}{2\pi(1-\nu)}$$

in terms of the Burgers vector b . These infinite sums are conveniently evaluated by application of the Residue Theorems of complex function theory, i.e.

$$\sum_{j=-\infty}^{+\infty} f(j) = -\sum \text{res}\{\pi f(z) \cot \pi z\}. \quad (C5)$$

For instance, for σ_{11} according to (C2), the function $f(z)$ has a double pole for $(z+\xi)-i\eta = 0$ ($i^2 = -1$) with associated residue

$$\begin{aligned} \text{res} &= \lim_{z \rightarrow -\xi+i\eta} \frac{d}{dz} \left\{ \frac{\eta[3(\xi+z)^2 + \eta^2]}{[(\xi+z)^2 + \eta^2]^2} \pi \cot \pi z \right\} \\ &= -i\pi \cot \pi(-\xi+i\eta) - \frac{1}{2}\eta\pi^2 \csc^2 \pi(-\xi+i\eta). \end{aligned}$$

Similarly, one obtains the residue corresponding to the other double pole for $(z+\xi)+i\eta = 0$. Then,

$$\begin{aligned} \sum_{j=-\infty}^{+\infty} \frac{\eta[3(\xi+j)^2 + \eta^2]}{[(\xi+j)^2 + \eta^2]^2} \\ = -\frac{2\pi \sinh 2\pi\eta}{\cosh 2\pi\eta - \cos 2\pi\xi} - \eta\pi^2 \left\{ \frac{\sin^2 \pi\xi \cosh^2 \pi\eta - \cos^2 \pi\xi \sinh^2 \pi\eta}{(\sin^2 \pi\xi + \sinh^2 \pi\eta)^2} \right\}. \end{aligned}$$

After rearrangement, the result for σ_{11} , along with the results for the other stress components obtained similarly, reads

$$\sigma_{11} = \frac{a}{h} \pi \frac{1}{\cosh 2\pi\eta - \cos 2\pi\xi} \left\{ 2 \sinh 2\pi\eta + 2\pi\eta \frac{1 - \cos 2\pi\xi \cosh 2\pi\eta}{\cosh 2\pi\eta - \cos 2\pi\xi} \right\} \quad (C6)$$

$$\sigma_{22} = -\frac{a}{h}\pi \left\{ 2\pi\eta \frac{1 - \cos 2\pi\xi \cosh 2\pi\eta}{(\cosh 2\pi\eta - \cos 2\pi\xi)^2} \right\} \quad (C7)$$

$$\sigma_{12} = -\frac{a}{h}\pi \frac{\sin 2\pi\xi}{\cosh 2\pi\eta - \cos 2\pi\xi} \left\{ 1 - 2\pi\eta \frac{\sinh 2\pi\eta}{\cosh 2\pi\eta - \cos 2\pi\xi} \right\}. \quad (C8)$$

The displacement field due to a string of dislocations cannot be constructed directly along the same lines. The reason for this is that the displacement component u_2 perpendicular to the slip plane increases without bound when the distance from the dislocation increases [see (14)]. This difficulty is overcome by adding a string of dislocations with the opposite sign on the same slip plane, as illustrated in figure C1; this is consistent with the restriction imposed in the present analyses that all dislocations come in dipoles (see section 2.3). For a dipole, the displacements do remain bounded, as is readily verified by adding the displacement fields according to (13) and (14) for a positive and a negative dislocation. Now consider the dipole j formed by dislocation j (Burgers vector b) and the opposite dislocation at a distance ΔX ahead of it. The displacement components u_α at x_α due to all such dipoles are obtained as

$$u_1 = c \sum_{j=-\infty}^{+\infty} \left\{ \frac{1}{2} \left[\frac{(\xi + j)\eta}{(\xi + j)^2 + \eta^2} - \frac{(\xi + \Delta\xi + j)\eta}{(\xi + \Delta\xi + j)^2 + \eta^2} \right] + (1 - \nu) \tan^{-1} \left(\frac{\Delta\xi\eta}{(\xi + j)(\xi + \Delta\xi + j) + \eta^2} \right) \right\} \quad (C9)$$

$$u_2 = c \sum_{j=-\infty}^{+\infty} \left\{ \frac{1}{2} \left[\frac{\eta^2}{(\xi + j)^2 + \eta^2} - \frac{\eta^2}{(\xi + \Delta\xi + j)^2 + \eta^2} \right] - \frac{1}{4} (1 - 2\nu) \ln \frac{(\xi + j)^2 + \eta^2}{(\xi + \Delta\xi + j)^2 + \eta^2} \right\} \quad (C10)$$

where

$$\Delta\xi = \Delta X/d$$

and

$$c = \frac{b}{2\pi(1 - \nu)}.$$

The two sums in the respective square brackets in (C9) and (C10) are directly evaluated by using

$$\sum_{j=-\infty}^{+\infty} \frac{(\xi + j)\eta}{(\xi + j)^2 + \eta^2} = \frac{1}{2} \frac{2\pi\eta \sin 2\pi\xi}{\cosh 2\pi\eta - \cos 2\pi\xi} \quad (C11)$$

$$\sum_{j=-\infty}^{+\infty} \frac{\eta^2}{(\xi + j)^2 + \eta^2} = \frac{1}{2} \frac{2\pi\eta \sinh 2\pi\eta}{\cosh 2\pi\eta - \cos 2\pi\xi} \quad (C12)$$

but the remaining sums in both expressions require special care.

For that purpose we note that sums as in the left-hand side of (C5) can also be evaluated through

$$\sum_{j=-\infty}^{+\infty} f(j) = \int \left\{ \sum_{j=-\infty}^{+\infty} F(j) \right\} d\eta \quad (\text{C13})$$

if $F(j)$ is defined as $F(j) = \partial f(j)/\partial \eta$, under certain restrictions concerning $f(j)$. For the last sum in (C10) we have

$$F(j) = \frac{2}{\eta} \left\{ \frac{\eta^2}{(\xi + j)^2 + \eta^2} - \frac{\eta^2}{(\xi + \Delta\xi + j)^2 + \eta^2} \right\}$$

in which we recognize the separate contributions of the two opposite dislocations at ξ and at $\xi + \Delta\xi$, respectively. Each of the two terms can now be summed separately by making use of (C12); after integration, (C13) gives

$$\sum_{j=-\infty}^{+\infty} \ln \frac{(\xi + j)^2 + \eta^2}{(\xi + \Delta\xi + j)^2 + \eta^2} = \ln \frac{\cosh 2\pi\eta - \cos 2\pi\xi}{\cosh 2\pi\eta - \cos 2\pi(\xi + \Delta\xi)}. \quad (\text{C14})$$

Similarly, for the last sum in (C9) we have

$$F(j) = \frac{\Delta\xi[(\xi + j)(\xi + \Delta\xi + j) - \eta^2]}{[(\xi + j)(\xi + \Delta\xi + j) + \eta^2]^2 + (\Delta\xi\eta)^2}$$

for which the Residue Theorem (C5) yields

$$\sum_{j=-\infty}^{+\infty} F(j) = \pi \frac{\sin 2\pi\xi}{\cosh 2\pi\eta - \cos 2\pi\xi} - \pi \frac{\sin 2\pi(\xi + \Delta\xi)}{\cosh 2\pi\eta - \cos 2\pi(\xi + \Delta\xi)}$$

so that, after integration, we find from (C13) that

$$\begin{aligned} \sum_{j=-\infty}^{+\infty} \tan^{-1} \left(\frac{\Delta\xi\eta}{(\xi + j)(\xi + \Delta\xi + j) + \eta^2} \right) \\ = -\tan^{-1} \left(\frac{\tan \pi\xi}{\tanh \pi\eta} \right) + \tan^{-1} \left(\frac{\tan \pi(\xi + \Delta\xi)}{\tanh \pi\eta} \right). \end{aligned} \quad (\text{C15})$$

We note that even though the summations could only be carried out by considering dipoles of dislocations, the contributions of the opposite dislocations are still recognized separately in (C14) and (C15). This enables one to separate out the displacement fields for the two opposite strings of dislocations, and to write the result for the original string of dislocations with Burgers vectors b as

$$u_1 = c \left\{ \frac{1}{4} \frac{2\pi\eta \sin 2\pi\xi}{\cosh 2\pi\eta - \cos 2\pi\xi} - (1 - \nu) \tan^{-1} \left(\frac{\tan \pi\xi}{\tanh \pi\eta} \right) \right\} \quad (\text{C18})$$

$$u_2 = c \left\{ \frac{1}{4} \frac{2\pi\eta \sinh 2\pi\eta}{\cosh 2\pi\eta - \cos 2\pi\xi} - \frac{1}{4} (1 - 2\nu) \ln(\cosh 2\pi\eta - \cos 2\pi\xi) \right\} \quad (\text{C19})$$

(provided, of course, that there is an opposite string of dislocations available). The last complication that needs to be dealt with is the discontinuity in u_1 at $\xi = \pm \frac{1}{2}$, which gives rise to a jump $u_1(\frac{1}{2}, \eta) - u_1(-\frac{1}{2}, \eta) = -\frac{1}{2}b \operatorname{sgn}(\eta)$. Obviously, this is an artifact caused by the fact that \tan^{-1} is a multivalued function. This can be resolved by adding a term

$$-\delta \frac{b}{2} \operatorname{sgn}(\eta)$$

to the right-hand side in (C18), where $\delta = +1$ if $\frac{1}{2} < \xi < \frac{3}{2}$ and $\delta = -1$ if $-\frac{3}{2} < \xi < -\frac{1}{2}$. This renders the u_1 field continuous over all $\xi \in (-1, 1)$.

It should be noted that the analytical summations considered here are generally very efficient, since some of the series converge very slowly. For example, when the sum in (C14) is approximated for, say, $\xi = 0.0125$, $\Delta\xi = 0.925$, $\eta = -0.5$ by a finite sum from $-k$ to $+k$, it turns out that one needs to take k as large as 10000 in order to arrive within 2.5% of the analytical result in (C14).

The above results for the stresses and displacements due to an infinitely long string of dislocations can be immediately applied to the analysis (see section 3) of the periodic array of cells illustrated in figure 4 by taking d to be equal to $2w$. Using the substitutions $\xi = -\frac{1}{2}\Delta\xi_1$ and $\eta = -\frac{1}{2}\Delta\xi_2$ for the i th dislocation in the unit cell (cf. (22)), one arrives at the expressions (19)–(21) and (23)–(24), respectively.

References

- [1] Gulluoglu A N, Srolovitz D J, LeSar R and Lomdahl P S 1989 *Scr. Metall.* **23** 1347
- [2] Amodeo R J and Ghoniem N M 1990 *Phys. Rev. B* **41** 6958
- [3] Amodeo R J and Ghoniem N M 1990 *Phys. Rev. B* **41** 6968
- [4] Lepinoux J and Kubin L P 1987 *Scr. Metall.* **21** 833
- [5] Kubin L P, Canova G, Condat M, Devincere B, Pontikis V and Bréchet Y 1992 *Nonlinear Phenomena in Materials Science II* ed G Martin and L P Kubin (Vaduz: Sci-Tech) p 455
- [6] Gulluoglu A N and Hartley C S 1992 *Modelling Simul. Mater. Sci. Eng.* **1** 1
- [7] Gulluoglu A N and Hartley C S 1993 *Modelling Simul. Mater. Sci. Eng.* **1** 383
- [8] Lubarda V, Blume J A and Needleman A 1993 *Acta Metall. Mater.* **41** 625
- [9] Fang X F and Dahl W 1993 *Mater. Sci. Eng. A* **164** 300
- [10] Groma I and Pawley G S 1993 *Mater. Sci. Eng. A* **164** 306
- [11] Walgraef D and Aifantis E C 1985 *J. Appl. Phys.* **58** 688
- [12] Aifantis E C 1986 *Mater. Sci. Eng.* **81** 563
- [13] De Borst R 1993 *Comput. Methods, Appl. Mech. Eng.* **103** 347
- [14] Fleck N A and Hutchinson J W 1993 *J. Mech. Phys. Solids* **41** 1825
- [15] Vitek V 1992 *Prog. Mater. Sci.* **36** 1
- [16] Arias T A and Joannopoulos J D 1994 *Phys. Rev. Lett.* **73** 680
- [17] Gallego R and Ortiz M 1993 *Modelling Simul. Mater. Sci. Eng.* **1** 383
- [18] Choi H C, Schwartzman A F and Kim K-S 1992 *Mater. Sci. Symp. Proc.* **239** 419
- [19] Peirce D, Asaro R J and Needleman A 1983 *Acta Metall.* **31** 1951
- [20] Nabarro F R N 1967 *Theory of Crystal Dislocations* (Oxford: Oxford University Press)
- [21] Hirth J P and Lothe J 1968 *Theory of Dislocations* (New York: McGraw-Hill)
- [22] Blume J A 1993 Private communication
- [23] Hill R 1963 *J. Mech. Phys. Solids* **11** 357
- [24] Van der Giessen E and Needleman A 1994 *Computational Material Modeling ASME AD vol 42/PVP vol 294*, ed A K Noor and A Needleman (New York: ASME) p 53
- [25] Asaro R J 1983 *Adv. Appl. Mech.* **23** 1
- [26] Bassani J L 1994 *Adv. Appl. Mech.* **30** 191
- [27] Cuitiño A M and Ortiz M 1992 *Modelling Simul. Mater. Sci. Eng.* **1** 225
- [28] Seeger A 1957 *Dislocations and Mechanical Properties of Crystals* (New York: Wiley) p 243
- [29] Basinski Z S 1959 *Phil. Mag.* **4** 343
- [30] Drucker D C 1965 *High Strength Materials* ed V F Zackey (New York: Wiley)
- [31] Wang H Y and LeSar R 1995 $O(N)$ algorithm for dislocation dynamics *Phil. Mag. A* **71** 149